

Paleoceanography and Paleoclimatology



RESEARCH ARTICLE

10.1029/2022PA004414

Key Points:

- The climate over the central Mediterranean shifted from a cool-arid to a humid regime during the Early Miocene around 19.0 Ma
- The transition to more humid conditions may have been a consequence of the first Miocene restriction of the Mesopotamian Seaway (MSR-1)
- Circulation changes in the proto-Mediterranean coupled with changes in the sedimentation may have terminated regional phosphorite episodes

Supporting Information:

Supporting Information may be found in the online version of this article.

Correspondence to:

R. Zammit,
zammitR2@cardiff.ac.uk;
raymond.zammit@um.edu.mt

Citation:




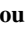



Zammit, R., Lear, C. H., Samankassou, E., Lourens, L. J., Micallef, A., Pearson, P. N., & Bialik, O. M. (2022). Early Miocene intensification of the North African hydrological cycle: Multi-proxy evidence from the shelf carbonates of Malta. *Paleoceanography and Paleoclimatology*, 37, e2022PA004414. <https://doi.org/10.1029/2022PA004414>

Received 26 JAN 2022
 Accepted 6 SEP 2022

Author Contributions:

Conceptualization: R. Zammit, C. H. Lear, O. M. Bialik
Formal analysis: R. Zammit, E. Samankassou
Funding acquisition: R. Zammit, C. H. Lear, O. M. Bialik
Investigation: R. Zammit, C. H. Lear, E. Samankassou, L. J. Lourens, A. Micallef, P. N. Pearson, O. M. Bialik

Early Miocene Intensification of the North African Hydrological Cycle: Multi-Proxy Evidence From the Shelf Carbonates of Malta

R. Zammit¹ , C. H. Lear¹ , E. Samankassou² , L. J. Lourens³ , A. Micallef^{4,5} , P. N. Pearson¹ , and O. M. Bialik⁴ 

¹School of Earth and Environmental Sciences, Cardiff University, Cardiff, UK, ²Department of Earth Sciences, University of Geneva, Geneva, Switzerland, ³Faculty of Geosciences, Utrecht University, Utrecht, The Netherlands, ⁴Department of Geosciences, University of Malta, Msida, Malta, ⁵Helmholtz Centre for Ocean Research Kiel, Kiel, Germany

Abstract During the Miocene (23.0–5.3 Ma) North Africa experienced both humid and arid intervals, but the underlying cause of these transitions is unknown. Earth's climate was characterized by a unipolar icehouse with a dynamic Antarctic ice sheet, which may have influenced regional hydrology through atmospheric teleconnections. However, the Miocene also witnessed the restriction of the Mesopotamian Seaway, which may have had significant climatic impacts. The Maltese il-Blata section (Central Mediterranean) comprises Late Oligocene to Early Miocene marine deposits previously used to constrain the timing of the Mesopotamian Seaway restriction using the ϵNd tracer. The location of this section also makes it sensitive to climatic changes in the North African region, and biogeochemical changes in the central Mediterranean. Here, we present lithological and geochemical records of the il-Blata section. We find a marked shift in lithology and an increase in sedimentation rate coeval with the Early Miocene (~19–20 Ma) restriction of the Mesopotamian Seaway. Concomitant changes in bulk sediment CaCO_3 , Sr/Ca, K/Al, Ti/Al, Zr/Al, and Si/Ti support a major humid climate transition and associated intensification of river systems over western North Africa. We propose that these changes in North African hydroclimate reflect either a tipping point effect in a gradually warming global climate, or are the result of the initial restriction of the Mesopotamian Seaway, perhaps through consequent changes in Atlantic Meridional Overturning Circulation and the West African Monsoon. We also suggest the restriction of the Mesopotamian Seaway inhibited phosphorite deposition at low latitudes.

Plain Language Summary The climate over the densely populated areas of North Africa and the Central Mediterranean is influenced by the West African Monsoon system. Climate data from the region is limited and models fail to make consistent predictions in the context of Anthropogenic global warming. Therefore, it is important to examine the geological past when atmospheric carbon dioxide levels were similar to values predicted for the end of the century. The il-Blata section in Malta (central Mediterranean) holds a geological record from 25 to 18 million years ago. This time interval is not well represented elsewhere in the region. Geological records from this section indicate a large increase in regional humidity around 19 million years ago. This humid transition followed a tectonic event that resulted in the closure of the Mesopotamian Seaway which connected the Indian Ocean with the Mediterranean Sea. This may reflect an important role for tectonic forcing in the evolution of the West African Monsoon system through changes in ocean circulation patterns. The change to a wetter climate also occurred against a backdrop of gradually warming global climate, so an alternative interpretation is that it reflects a regional tipping point in the climate system.

1. Introduction

1.1. Early to Mid-Miocene Climate

The Miocene epoch (20.03 Ma to 5.33 Ma) witnessed several important climate transitions (Figure 1), and has been proposed as a test-bed for exploring moderate to high $p\text{CO}_2$ climates (Steinhorsdottir et al., 2020). The Miocene is also a time of large scale tectonic changes that resulted in reorganization of ocean basins and subsequent changes in global heat transport (Hamon et al., 2013; Potter & Szatmari, 2009). The base of the Miocene (23.03 Ma) is marked by a transient glaciation event known as the Oligocene-Miocene Transition (OMT; Figure 1), during which the Antarctic Ice-Sheet advanced and retreated on orbital timescales (Mawbey & Lear, 2013; Miller et al., 1991; Mudelsee et al., 2014; Naish et al., 2001; Zachos et al., 2001). For around 3 million years following

© 2022. The Authors.

This is an open access article under the terms of the [Creative Commons Attribution License](https://creativecommons.org/licenses/by/4.0/), which permits use, distribution and reproduction in any medium, provided the original work is properly cited.

Methodology: R. Zammit, C. H. Lear, E. Samankassou, O. M. Bialik
Resources: R. Zammit, C. H. Lear, A. Micallef
Writing – original draft: R. Zammit
Writing – review & editing: R. Zammit, C. H. Lear, E. Samankassou, L. J. Lourens, A. Micallef, P. N. Pearson, O. M. Bialik

the OMT, the marine benthic foraminiferal oxygen isotope ($\delta^{18}\text{O}$) record exhibits a strong eccentricity signal (De Vleeschouwer et al., 2017; Liebrand et al., 2011) with rather consistent glacial and interglacial values and $\sim 1\%$ variability (Figure 1; Liebrand et al., 2011; Westerhold et al., 2020). This interval was terminated by an unusually warm interglacial at ~ 19.6 Ma, followed by an unusually cool glacial maximum at ~ 19.4 Ma (Figure 1). Between 19.4 and 17.0 Ma, both the glacial and interglacial values display a gradual warming trend (Figure 1; Cramer et al., 2009; De Vleeschouwer et al., 2017; Westerhold et al., 2020), followed by a relatively abrupt warming into the Miocene Climatic Optimum (MCO), which was also associated with the “Monterey” positive $\delta^{13}\text{C}$ isotope excursion (Diester-Haass et al., 2009, 2013; Holbourn et al., 2007; Sosdian et al., 2020; Vincent & Berger, 1985). The MCO was terminated by the middle Miocene climatic transition (MMCT), marked by declining $p\text{CO}_2$, a step-wise increase in $\delta^{18}\text{O}$ (14.6 Ma to 13.8 Ma) (Holbourn et al., 2014), and a permanent increase in global ice volume from 13.8 Ma (Abreu & Anderson, 1998; Flower & Kennett, 1994; Lear et al., 2015; Zachos et al., 2001). While the details of the climatic events of the OMT, MCO and the MMCT are becoming relatively well known, regional and global climate regimes between the OMT and the MCO (~ 23 to ~ 17 Ma) are currently poorly investigated despite modern to near-future CO_2 concentrations (Steinhorsdottir et al., 2020). Possible reasons for this include the limited number of sections that span this time interval without large hiatuses, as evidenced by the absence of base-Burdigalian and base-Langhian Global Boundary Stratotype Sections and Points (GSSPs) (Fabbrini et al., 2019; Foresi et al., 2011, 2014; Iaccarino et al., 2011; Gradstein et al., 2012, 2020).

1.2. Evolution of Mediterranean Climate During the Early Miocene

The present semi-enclosed nature of the Mediterranean Sea formed during the Miocene (Cornacchia et al., 2021; Kocsis et al., 2008; Rögl, 1999). Throughout the Cenozoic, the northward movement of the African and Arabian Plates continued to fragment the Tethys Ocean and generate smaller basins. This eventually resulted in the restriction of the Mesopotamian Seaway that connected the Indian Ocean to the proto-Mediterranean and led to the termination of low latitude circum-global halo-thermal circulation (de la Vara and Meijer, 2016). Recent work using the ϵNd tracer has revealed that the restriction of the Mesopotamian Seaway occurred in two distinct steps (Bialik et al., 2019). The initial Mesopotamian Seaway restriction (MSR-1) occurred during the Early

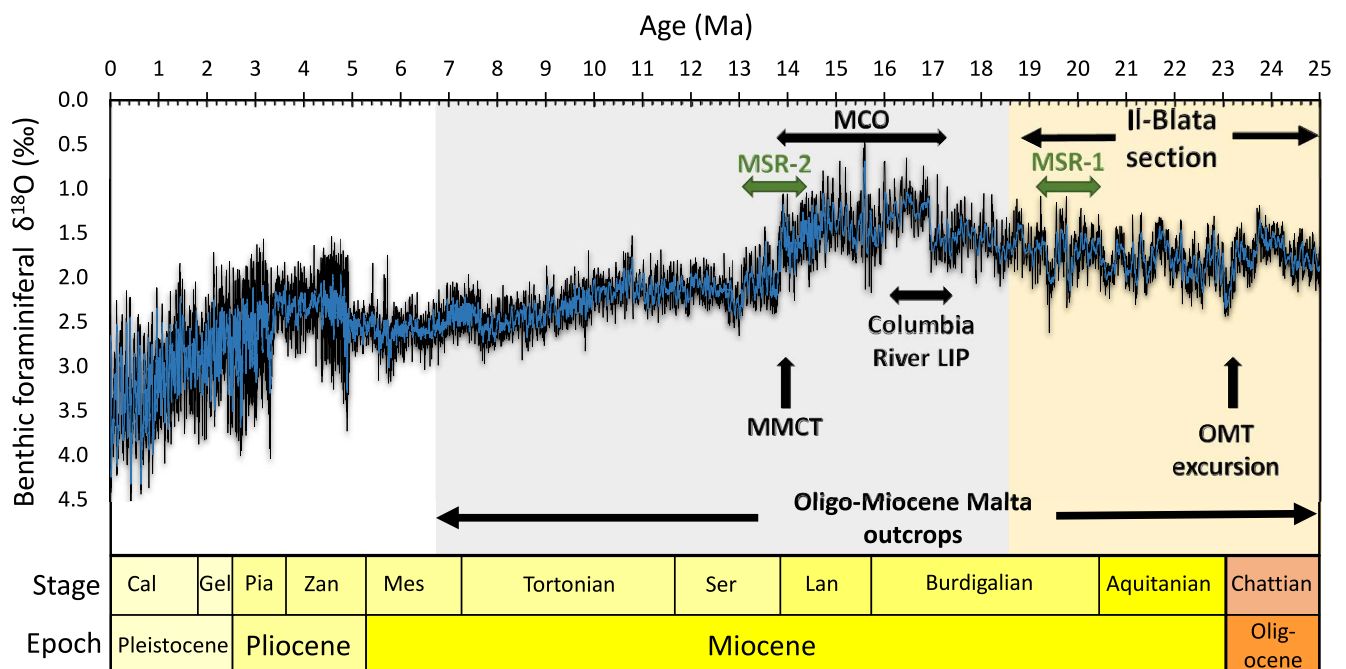


Figure 1. Benthic foraminiferal oxygen isotope compilation (Westerhold et al., 2020) of the last 25 Myr and significant oceanographic and climatic events during this interval. The sedimentary deposits outcropping on the Maltese Islands were deposited during different climatic regimes from the Late Oligocene to the Late Miocene. The two major steps of the Mesopotamian Seaway restriction are highlighted [MSR-1 and MSR-2, the latter coinciding with the Middle Miocene Climate Transition (MMCT)]. Oligocene-Miocene transition (OMT), Large igneous province (LIP), Miocene Climatic Optimum (MCO). Abbreviations for stages: Lan - Langhian, Ser - Serravallian, Mes - Messinian, Zan - Zanclean, Pia - Piacenzian, Gel - Gelasian, Cal - Calabrian.

Miocene ~ 20 Ma, while the final complete disconnection (MSR-2) occurred during the MMCT (~ 13.8 Ma) (Bialik et al., 2019). Intermittent reconnections and pre MSR-1 flow levels may have occurred between these two steps (Cornacchia et al., 2018; Sun et al., 2021).

In addition to these large scale tectonic and circulation changes, the Mediterranean region also shifted from a warm arid to a warm humid climate during the Early to Middle Miocene (John et al., 2003). However, the timing of this climatic shift is uncertain. John et al. (2003) noted a significant increase in the kaolinite/smectite ratio of sediments in Malta, and used an oxygen and carbon isotope stratigraphy to infer that the transition to more humid conditions and intense chemical weathering occurred close to the onset of the MCO at ~ 17 Ma. It has been suggested that the clay rich interval (CRI) in the Maltese Upper Globigerina Limestone member (UGLm) represents fully humid conditions (John et al., 2003). Subsequent age models (Mourik et al., 2011) suggest that the CRI, and hence the establishment of the humid phase, occurred later, at around 14.6 Ma. The North African humid climate regime intensified further after the MMCT at 13.8 Ma (John et al., 2003). It has been suggested that this increase in humidity was due to a northward migration of the ITCZ over Africa in response to cooling and ice growth in Antarctica (John et al., 2003; Mutti et al., 2006). However, the Early and middle Miocene restriction events of the Mesopotamian Seaway raise the possibility of a tectonically mediated mechanism. Understanding the mechanisms behind past changes in hydrology of the North African region is important because this region is currently poorly constrained in future climate simulations (Masson-Delmotte et al., 2021).

1.3. Study Site (Malta) and Objectives

The pelagic to hemi-pelagic phosphorite bearing deposits of the Maltese Islands have repeatedly provided a reliable lithological, paleontological and geochemical record of regional and global climatic and oceanographic changes during the late Oligocene (c. 28 to 23 Ma) and throughout the Miocene (23–5.3 Ma) (Abels et al., 2005; Badger et al., 2013; Bialik et al., 2019, 2021; Hilgen et al., 2009; Jacobs et al., 1996; Mourik et al., 2011). The Maltese Islands, located on an isolated carbonate platform at the northern edge of the African plate (Figure 2), provide an opportunity to investigate changes in the hydrological regime over North Africa during the Oligo-Miocene. Here we present high-resolution lithostratigraphic and geochemical records from the Late Oligocene through Early Miocene il-Blata section outcropping along the south-west coast of Malta (Figure 2). We also construct a new age model for this site based on $^{87}\text{Sr}/^{86}\text{Sr}$. This allows us to confirm the temporal correlation of the phosphorite deposits at il-Blata (Baldassini & Di Stefano, 2015; Föllmi et al., 2008) with the deposition of the global low latitude Late Oligocene to Early Miocene phosphorites (Schöllhorn et al., 2019). We use a multiproxy approach to infer changes in the sedimentation rate and paleoceanographic conditions at il-Blata during the Early Miocene. Calcium concentrations and CaCO_3 [%] are used to quantify the marine carbonate component in the sediment. Aluminium normalized proxies are used to indicate changes in fluvial and aeolian sediment fluxes (Ti/Al, Zr/Al) and chemical weathering intensity (K/Al), while Si/Ti ratios are used to infer changes in paleoproductivity. Sulphur concentrations are used to assess paleoredox conditions, and bulk sediment Sr/Ca reflects the supply of shelf carbonate to the system, acting as a local sea-level indicator. We show that the regional hydrology shifted to more humid conditions ~ 19 Ma. This coincided with the initial restriction of the Mesopotamian Seaway during a time of general warming climate. We explore possible mechanisms for this change, which probably also caused the cessation of major phosphorite deposition in this region.

2. Materials and Methods

2.1. Study Site and Field Sampling

The Maltese Islands rest on the NE side of the Pantelleria rift, a deep trough that runs NE-SW for 100 km between the island of Sicily and the Tunisian tip of North Africa (Dart et al., 1993) (Figure 2). The Oligo-Miocene il-Blata section outcrops along the SW coast of the Island of Malta (Figure 2). The section is exposed along a slope (base at 35.9004°N , 14.3309°E , top at 35.9000°N , 14.3314°E) and is almost identical to the section described by Baldassini and Di Stefano. (2015). During sampling, the first few cm of the oxidized surface was removed using a hammer, and the samples were collected from the visibly unoxidized part of the rock. Samples were wrapped in aluminium foil and placed in labeled plastic bags. It is highly unlikely that there was any significant aluminium contamination to our samples (Lewis & Christensen, 2016). Sampling intervals varied throughout the section, ranging from one sample every 10 cm to one sample every 50 cm depending on the accessibility of the outcrop. In total, 142 samples were collected from a ~ 40 m section of the Globigerina Limestone formation (GLfm).

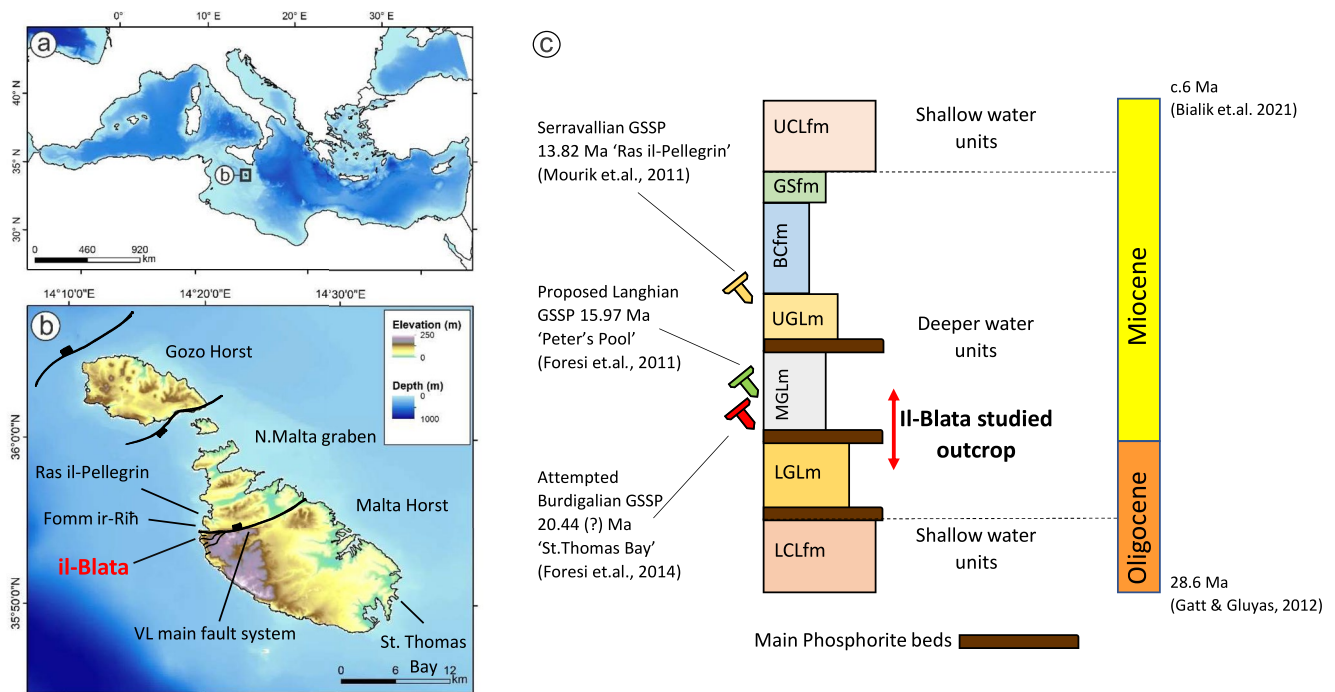


Figure 2. (a) The Maltese Archipelago lies in the central Mediterranean on the northern margin of the African plate. (b) The Maltese Islands represent the exposed part of a complex Oligo-Miocene tectonic regime dominated by a NE to SW trending horst-graben system (Dart et al., 1993). The il-Blata study site lies at the edge of the North Malta graben close to the Victoria Lines main fault system. The Langhian-Serravallian GSSP at the Ras il-Pellegrin section lies across the Fomm ir-Riħ embayment to the north of the study site. The St. Thomas Bay section has been considered a candidate for the Burdigalian GSSP (Foresi et al., 2014). (c) General lithostratigraphy of the Maltese Islands. LCLfm—Lower Coralline Limestone formation, LGLm—Lower Globigerina Limestone member, MGLm—Middle Globigerina Limestone member, UGLm—Upper Globigerina Limestone member, BCfm—Blue Clay formation, GSfm—Green Sand formation, UCLfm—Upper Coralline Limestone formation.

2.2. Geochemistry and Microfossils

2.2.1. Percentage Carbonate

The percentage carbonate of all samples was measured using a digital calcimeter. About 1 g of powdered, homogenised, and dried sample was weighed and transferred to a 50 ml sample bottle. A clean, dry glass cuvette was filled with 6 M HCl, placed in the bottle, and connected to a FOGL digital calcimeter. The digital calcimeter was standardised using an in-house carbonate standard with average precision of 2% (1 s.d.).

2.2.2. Stable Isotope Stratigraphy

Approximately 5 g of bulk sediment material was crushed and homogenised using an agate pestle and mortar and dried for 24 hr at 40°C. Carbon and oxygen isotope ratios were measured on ~500 µg of this powder using a Gasbench II coupled to a Thermo Delta V Advantage isotope ratio mass spectrometer at the School of Earth and Environmental Sciences, Cardiff University. Results are expressed in ‰ using the δ-notation on the Vienna Pee Dee Belemnite (VPDB) scale. The long-term precision of an in-house carbonate standard is ≤0.06 ‰ (1 s.d.) for δ¹⁸O and ≤0.05 ‰ for δ¹³C.

2.2.3. Major Elements

A total of 114 samples of the crushed and dried samples were selected for major element analysis using X-ray fluorescence. Analysis was performed using a hand-held Olympus Delta Innov-X XRF gun at the School of Earth and Environmental Sciences, Cardiff University. The instrument was standardised using in-house carbonate and silica standards. The following ratios were calculated to act as paleoproxies: Ti/Al and Zr/Al for aeolian flux (Govin et al., 2012; Hennekam et al., 2015; Krom et al., 1999; Martín-Puertas et al., 2010; Martínez-Ruiz et al., 2015), Sr/Ca for sea-level controlled export of shelf carbonate material (Bialik et al., 2020), K/Al for chemical weathering (Clift et al., 2014), and Si/Ti for biogenic silica production (Brown et al., 2007; Kylander et al., 2011). The bulk [Ca] was used to indicate the marine carbonate component while the bulk [S] indicates

redox conditions (Filippidi & Lange, 2019; Passier & de Lange, 1998; Wei et al., 2009). All X-ray fluorescence data are semi-quantitative.

2.2.4. Radiogenic Strontium Isotopes

A total of 16 samples were collected from the succession for strontium isotope analysis. The samples were selected as close as possible to the main sedimentary hiatuses observed in the field in order to time constrain the different sedimentary packages (Figure 3). For each sample, 30 mg of powdered bulk sediment was dissolved in 2.2 M high-purity acetic acid for 1–2 hr at room temperature (22–24°C) in conical 2 ml vials. The solutions were centrifuged, and the supernatant was recovered and transferred to Teflon vials, where it was dried to a residue on a hot plate. The residue was re-dissolved in 14 M HNO₃ and dried again prior to Sr separation from the matrix using Sr-Spec resin. The Sr separate was re-dissolved in 5 ml ~2% HNO₃ solution, and the ratios were measured using a Thermo Neptune PLUS Multi-Collector inductively coupled plasma mass spectrometer in static mode at the University of Geneva. The ⁸⁸Sr/⁸⁶Sr ratio (8.375209) was used to monitor internal fractionation during the run. Interferences at masses 84 (⁸⁴Kr), 86 (⁸⁶Kr), and 87 (⁸⁷Rb) were corrected in-run by monitoring ⁸³Kr and ⁸⁵Rb. An SRM987 standard was used to check external reproducibility, which, on the long term (more than 100 measurements in one year), was 10 ppm. The internally corrected ⁸⁷Sr/⁸⁶Sr values were further corrected for external fractionation by a value of –0.025‰ per amu, because a systematic difference between measured and nominal standard ratios of the SRM987 of ⁸⁷Sr/⁸⁶Sr was 0.71024 (McArthur et al., 2001). The ⁸⁷Sr/⁸⁶Sr were converted into numerical ages using the LOWESS 5 fit (McArthur et al., 2012).

2.3. Microfossils

About 10 g of sample was broken and placed into jars filled with deionized water and rotated on a vertical spinner for about 12–14 hr. Samples that remained strongly lithified following spinning were broken down using pestle and mortar and subsequently dried. All samples were dry sieved and examined with a binocular microscope in order to determine the presence of foraminifera.

3. Results

3.1. Lithostratigraphy

The lithostratigraphy of the studied section (Figure 3) is broadly similar to that described in previous studies for the il-Blata section (Baldassini & Di Stefano, 2015) and the related Fomm ir-Rih section (Föllmi et al., 2008; Gruszczynski et al., 2008; Jacobs et al., 1996). The description of the Middle Globigerina Limestone member (MGLm) given here is more detailed than previous descriptions and, together with geochemical records and a robust age model, offers a new perspective for the interpretation of the Maltese depositional intervals in relation to Early Miocene oceanographic, tectonic, and regional climate changes. We divide the studied section into two intervals, which we term Depositional Interval 1 and Depositional Interval 2. This subdivision is based on general field observations (color, grain size, weathering features, lithology, and abundance of phosphatic beds) that indicate a significant depositional change at around 11 m from the base of the studied section (Figure 3). Each interval is further subdivided into smaller sedimentary packages (SP) based on facies changes observed in the field.

3.1.1. Depositional Interval 1—Marine Carbonates and Phosphatic Deposits

In general, the lower 2 m of the section (SP I) is composed of highly weathered and bioturbated pale yellow wackestone/packstone facies associations within the Lower Globigerina Limestone member (LGLm; Figures 3 and 4a). This is capped by the ubiquitous condensed bed C₁ (Pedley & Bennett, 1985, Figure 4a). The beds toward the top of SP I display an increase in burrowing activity (*Thalassinoides*), an increase in broken *Pecten* bivalve shells, and a general increase in coarser grained material (Figure 4a). The base of C₁ is taken as the top of SP I.

The next sedimentary package (SP II) consist of the C₁ bed and the overlying 4.5 m of fine grained, bedded, pale-gray mudstone/wackestone facies associations pertaining to the Middle Globigerina Limestone member (MGLm) (Figures 3 and 4b). This package displays coarsening upwards and terminates with a shallowing sequence of *Thalassinoides* ichonofacies, broken macrofossils, a 20 cm thick preferentially weathered horizon (Figure 4b) and small phosphatic pebbles.

The next package, (SP III) lies unconformably on SP II. Its base comprises a limestone terrace containing a complex network of *Thalassinoides* ichonofacies, an erosional surface and a bed containing small phosphatic

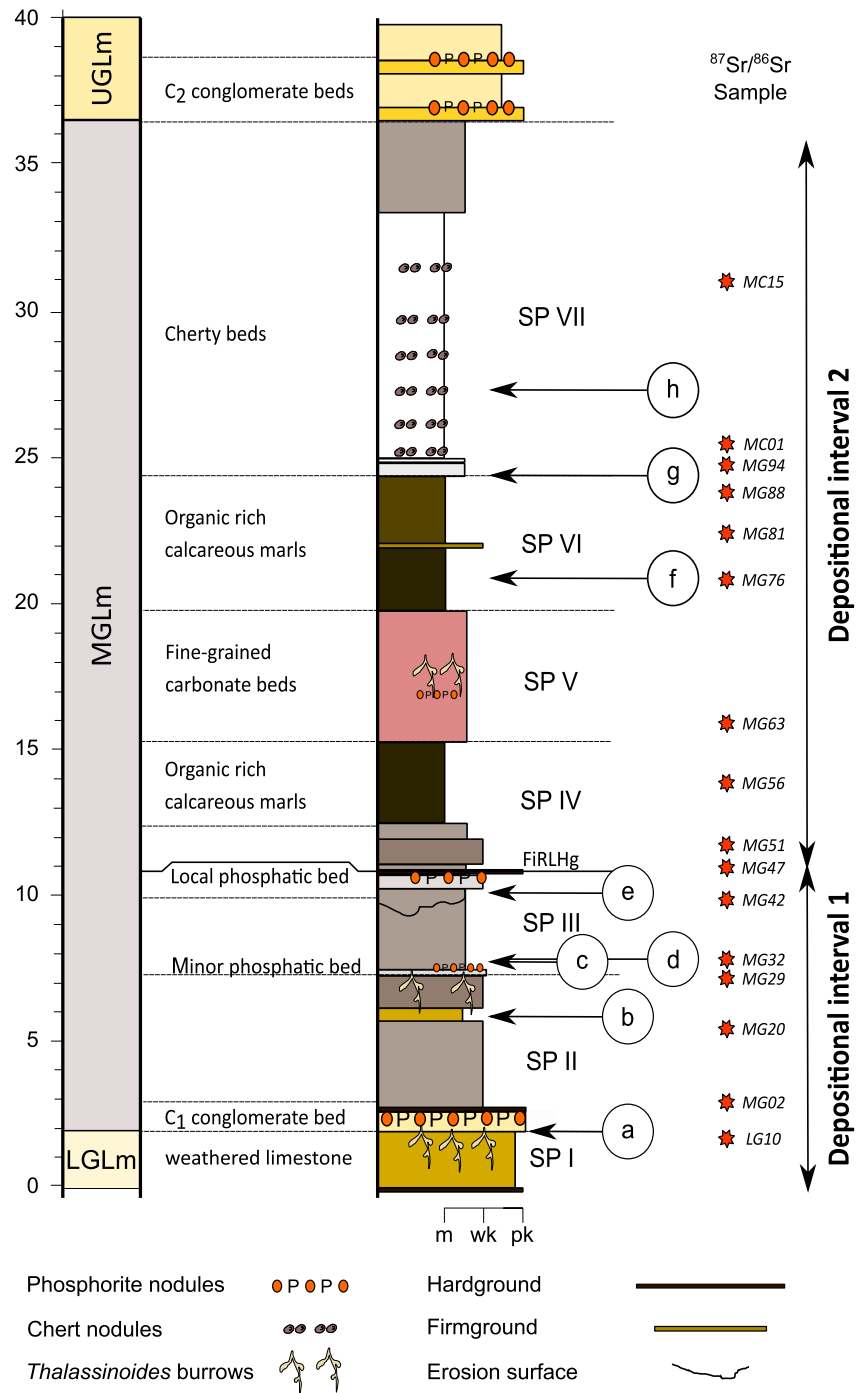


Figure 3. Lithostratigraphy of the il-Blata carbonate section pertaining to the Globigerina Limestone Formation. Fomm ir-Rih local hardground represents the ‘Fomm ir-Rih Local Hardground’ of Gruszczynski et al. (2008). Samples taken for $^{87}\text{Sr}/^{86}\text{Sr}$ dating are indicated by red stars and constrain the main sedimentary packages. SP—Sedimentary package, LGLm—Lower Globigerina Limestone member, MGLm—Middle Globigerina Limestone member, UGLm - Upper Globigerina Limestone member. Sample naming: LG—Lower Globigerina Limestone, MG—Middle Globigerina Limestone, MC—Middle Globigerina Limestone cherty interval.

pebbles (Figures 4b–4d). The overlying beds comprise 3 m of similar deposits to SP II. It is capped by an erosional surface (ES 1 *sensu* Baldassini & Di Stefano, 2015), which is filled by a phosphatic bed and capped by a phosphatic hardground (Figure 4e). We identify it as the Fomm ir-Rih local hardground (FiRLHg) described by Baldassini and Di Stefano. (2015). It is relatable to phosphatic hardgrounds identified by other authors (Föllmi

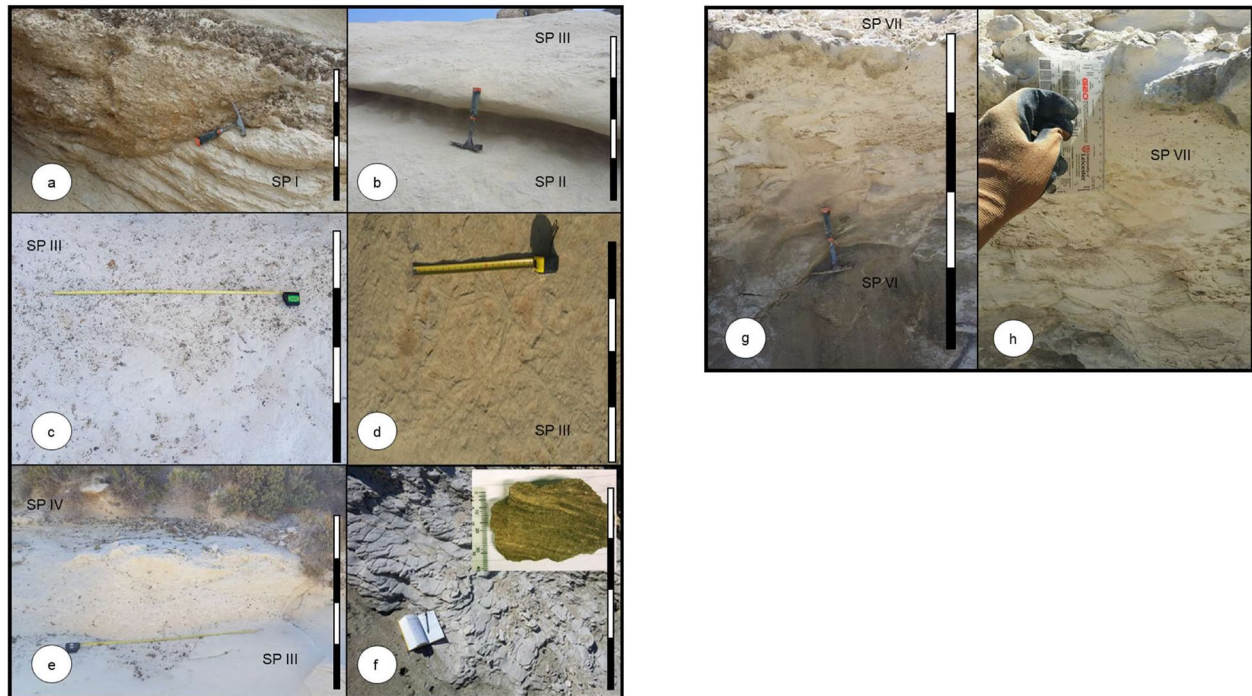


Figure 4. Sedimentological features of the il-Blata section. Black and white scale is 1 m. (a). Erosion surface at the top of SP I infill conglomerate material of gravity flow origin and phosphatic capping of the bed. (b). Notch between SP II and SP III. (c). Erosion feature followed by minor phosphatic interval at the base of SP III resting on top of limestone terrace. (d). *Thalassinoides* ichonofacies associated with limestone terrace at the base of SP III. (e). Erosion surface, phosphatic bed and planar hardground mark the end of depositional interval 1. (f). Dark, terrigenous-sediment rich mudstone facies SP VI, inset showing fine mm scale laminations. (g). Conformant transition from dark mudstones of SP VI to cherty deposits of SP VII transition. (h). Chert nodule SP VII.

et al., 2008; Gruszczynski et al., 2008). This package is followed by a sedimentary unconformity and indicates the possibility of a large hiatus (Figures 3 and 4e). Therefore, this unconformity was chosen to mark the top of Depositional Interval 1.

3.1.2. Depositional Interval 2—Calcareous Organic-Rich Marls and Cherty Deposits

The packages overlying the Fomm ir-Rih local hardground are significantly different from the underlying marine carbonates and have not previously been described in detail. Field observations indicate that, except for one unconformity at around 22 m from the base of the outcrop, this sequence is continuous. SP IV comprises 2.5 m of fine-grained dark gray/green organic rich calcareous marls (Figure 3). These are overlain by coarser grained reddish lime mudstones/wackestone facies (SP V; Figure 3). This package contains a horizon with small (~1 cm) allochthonous phosphatic pebbles at around 17 m above the base of the section, and evidence of bioturbation above this minor phosphatic layer. The transition to the next package (SP VI) is conformable. SP VI is similar to SP IV, and consists of finely laminated, dark, organic-rich calcareous marls (Figure 4f). A thin firmground (~2 cm width) occurs at 22 m above the base of the section. SP VI transitions conformably with a striking color change into a gray/white mudstone bed containing cm-scale siliceous intraclasts (Figures 4g and 4h). This transitional bed is capped by a thick band of chert nodules that weathers proud and defines the shift from the calcareous marls to the pale gray/white beds of SP VII (Figure 4h). SP VII consists of 9 m of very fine siliceous and carbonate sediment containing large chert nodules. The top of this package represents the termination of the studied section and is an unconformity that is capped by the yellow wackestone/packstone facies of the Upper Globigerina Limestone member (UGLm) and the associated C₂ phosphatic beds (Baldassini & Di Stefano, 2015, 2017; Pedley & Bennett, 1985).

3.2. Age Model and Sedimentation Rate

The 16 samples of bulk sediment analyzed for ⁸⁷Sr/⁸⁶Sr (Figure 3) display a generally consistent trend of increasing ⁸⁷Sr/⁸⁶Sr with height in the section, giving us confidence in using these data to obtain a reliable age model.

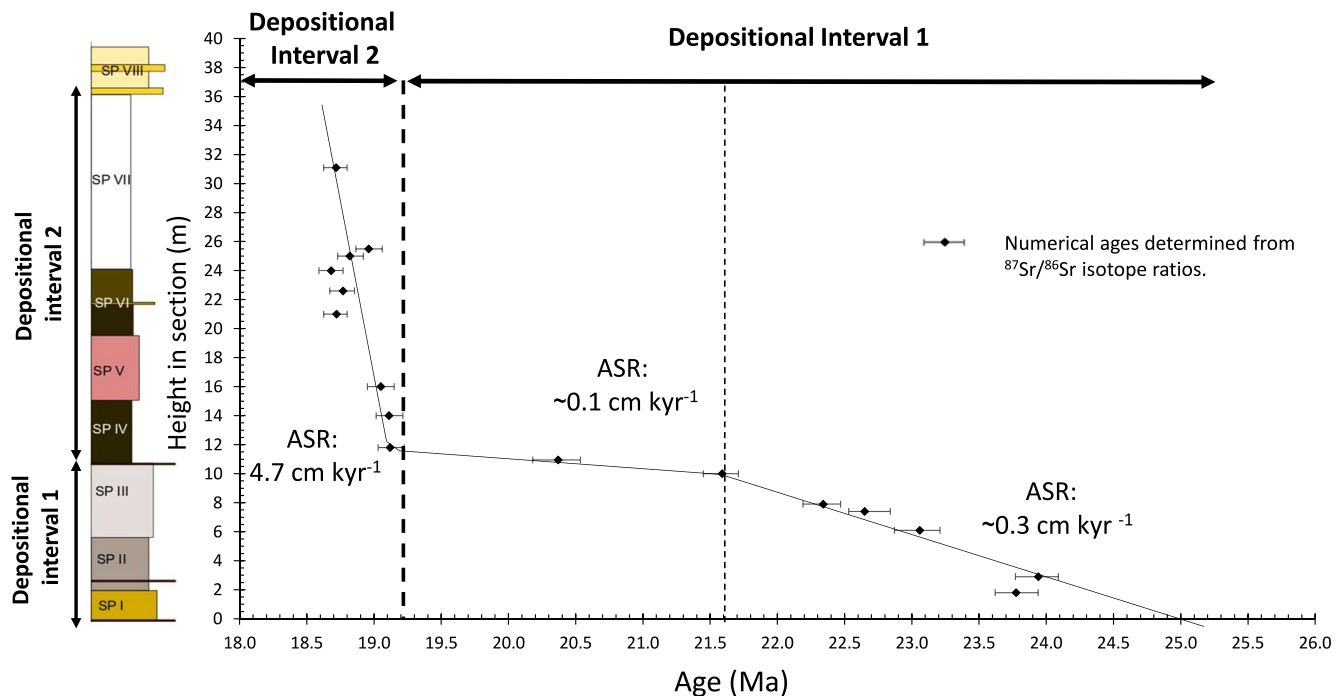


Figure 5. Numerical ages determined from $^{87}\text{Sr}/^{86}\text{Sr}$ ratios using LOWESS fit 5 model of McArthur et al. (2012) with respect to height in the il-Blata section. Simplified graphic log relates the height in section with the main sedimentary packages. The average sedimentation rate increases by an order of magnitude from Depositional Interval 1 to Depositional Interval 2. Average sedimentation rate (ASR).

The lowest $^{87}\text{Sr}/^{86}\text{Sr}$ value (0.708209) was recorded at 2.9 m above the base of the section (sample MG02), while the highest $^{87}\text{Sr}/^{86}\text{Sr}$ value (0.708515) was recorded at 24.0 m above the base of the section (sample MG88). The $^{87}\text{Sr}/^{86}\text{Sr}$ values suggest that the section was deposited between 24.9 Ma and 18.6 Ma (McArthur et al., 2012).

We note that this $^{87}\text{Sr}/^{86}\text{Sr}$ age model is in generally good agreement with the published nannofossil biostratigraphy of Baldassini and Di Stefano (2015) for this section. The main points of disagreement between our age model and the nannofossil record of Baldassini and Di Stefano. (2015) relate to the duration of Depositional Interval 1. The termination of Depositional Interval 1 is here determined to occur at 20.35 (+0.185, -0.170) Ma while the nannofossil record suggest a termination at ~ 21 Ma (no uncertainty provided) (Baldassini & Di Stefano, 2015). These discrepancies may be attributed to different sampling resolutions between the two studies and the difficulty in comparing the samples between the two studies due to the non-planar nature of the erosion surfaces at the site. Our $^{87}\text{Sr}/^{86}\text{Sr}$ data give an age of 19.121 (+0.102, -0.091) Ma to 18.526 (+0.085, -0.090) Ma for Depositional Interval 2, which is in excellent agreement with the nannofossil record (19.0 to 18.5 Ma) (Figure 5).

Our age model shows that the sedimentation rate during Depositional Interval 1 is on average 0.3 cm kyr^{-1} between 0 and 10.0 m followed by a condensed section at the top with a sedimentation rate of 0.1 cm kyr^{-1} . This increases significantly to an average 4.7 cm kyr^{-1} throughout Depositional Interval 2 (Figure 5).

3.3. Geochemistry

3.3.1. Bulk Carbonate Stable Isotopes

The bulk $\delta^{18}\text{O}$ and $\delta^{13}\text{C}$ records display a large negative excursion toward the top of SP I (Figure 6); this part of the record will not be discussed further since it can be attributed to meteoric diagenesis (Oehlert & Swart, 2014). In addition, the presence of ankerite has been shown to shift $\delta^{18}\text{O}$ to more positive values within the section (John et al., 2003). The bulk $\delta^{18}\text{O}$ record will therefore not be further discussed.

Starting at 4 m from the base of the section, the bulk sediment $\delta^{13}\text{C}$ displays a generally decreasing trend through SP II and III, before increasing by $\sim 0.4\%$ across the hiatus between Depositional Intervals 1 and 2. Bulk sediment $\delta^{13}\text{C}$ subsequently decreases through SP IV and SP V, reaching a minimum value at around 22.0 m from the

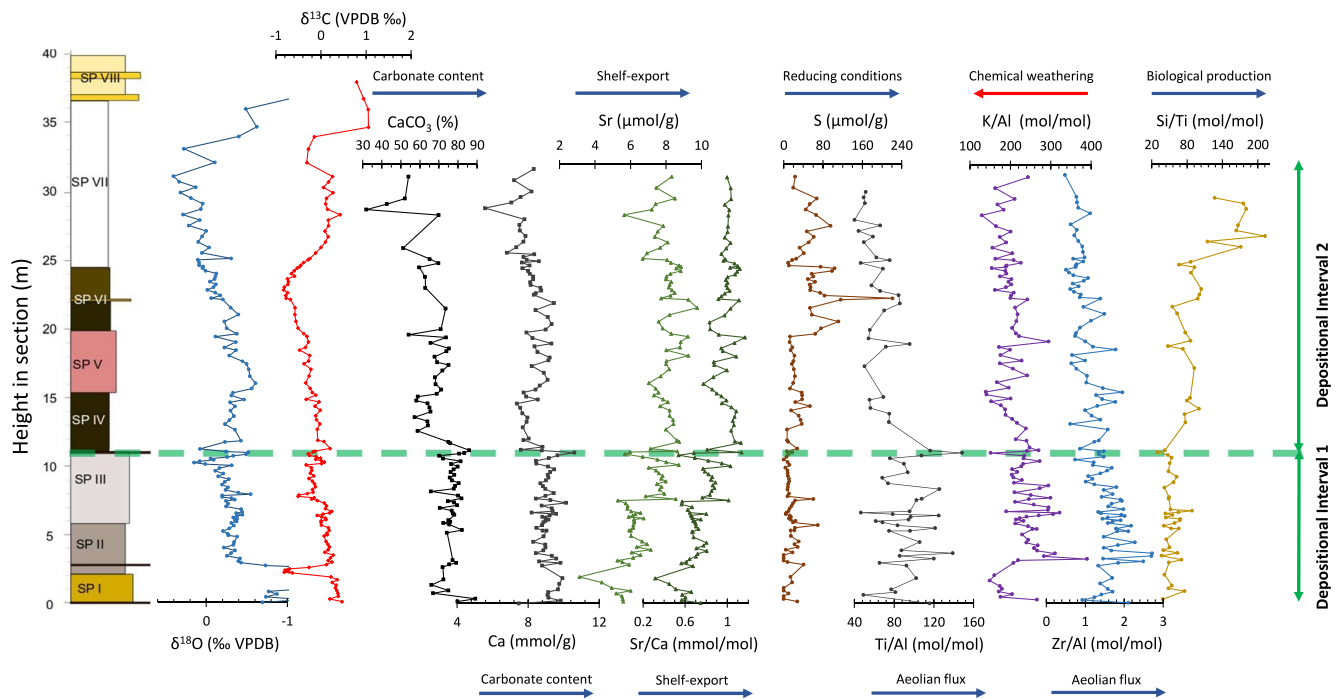


Figure 6. Bulk stable isotopes, %CaCO₃ (marine sediment component), elemental abundances of Ca, Sr, (control on the Ca/Sr ratio), S (redox) and ratios Sr/Ca (shelf-export), Ti/Al (aeolian flux), K/Al (chemical weathering), Zr/Al (aeolian flux), and Si/Ti (biogenic silica) with respect to height in section and lithology for the il-Blata section, Malta. Green dotted line delineates the hiatus between 20.0 Ma to 19.2 Ma and distinguishes the lithostratigraphy between the Depositional Interval 1 and Depositional Interval 2.

base, corresponding to an age of ~18.8 Ma and a minor local firmground. This is followed by a rapid rise of 1.2 ‰ within less than 0.15 Myr, reaching a maximum within the cherty beds of SP VII (Figure 6).

3.3.2. Carbonate Content

There is a marked difference in carbonate content between Depositional Interval 1 and Depositional Interval 2. Carbonate content is high (~80%) throughout Depositional Interval 1, decreases to ~60% in the lower part of Depositional Interval 2 (SP IV), and increases slightly through SP V. Carbonate content generally decrease through SP VI and SP VII with the lowest value (30%) recorded within the cherty SP VII layer (Figure 6).

3.3.3. Major Elements

Sediment [Ca] tends to covary with the carbonate record, reflecting the overall reduction in carbonate content from Depositional Interval 1 to Depositional Interval 2, with the lowest [Ca] occurring within the cherty layer SPVII (Figure 6). Bulk sediment Sr/Ca ratio covaries with bulk [Sr] except for a very short interval around 29 m from the base of the section (Figure 6). However, Sr/Ca does not covary with bulk δ¹⁸O, which is more susceptible to diagenetic influences. Bulk sediment Sr/Ca generally increases through the il-Blata section, with the main shifts associated with hiatuses and changes in sedimentary facies.

Bulk sediment [S] is generally very low and stable throughout Depositional Interval 1, after which an increase of ~40 µmol/g is recorded within SP IV, associated with a decrease in % carbonate and a general increase in clay content. A marked step increase of ~100 µmol/g coincides with the organic, clay rich interval of SP VI, with a notable spike (reaching values >200 µmol/g) around the firmground of Depositional Interval 2. Bulk sediment [S] decreases around the transition into the cherty interval but peaks around the middle of SP VII.

The Al normalized proxies Ti/Al, K/Al, and Zr/Al display a general decreasing trend from Depositional Interval 1 to Depositional Interval 2, likely reflecting the general increase in clay content up-section (Figures 6 and 8). Some of the values in interval 1 and interval 2 do overlap, however the average of these values changes from interval 1 to interval 2. The overlapping data points could reflect the inherent, short term climatic variability in the record (Figure 8). Bulk sediment Si/Ti records a step increase from Depositional Interval 1 to Depositional

Interval 2. During Depositional Interval 2, the ratio further increases within SP VI, and more steeply in SP VII (Figure 6). The data presented does not all have the same resolution since the concentration of some elements was below the detection limit in a number of samples.

3.4. Microfossils

All samples within Depositional Interval 1 were found to be strongly lithified and could only be disaggregated by mechanical means. On visual inspection of the sediment under a light microscope we found no planktonic foraminifera and only a few poorly preserved benthic foraminifera.

We were able to disaggregate many samples from Depositional Interval 2 without resorting to mechanical methods. In general, foraminifera are rare throughout Depositional Interval 2. No planktonic foraminifera were identified within the organic-rich sedimentary packages with very rare benthic specimens identified in the 100–250 μm size fraction. Very rare, well preserved planktic and benthic specimens were observed within the transitional bed between the organic-rich SP VI and the cherty SP VII. No specimens were found within the 250–355 μm size fraction for the cherty SP VII, while rare well-preserved benthic and planktic specimens were picked from the 100–255 μm size fraction. In general, within Depositional Interval 2, foraminifera tend to be very rare, well preserved, and small.

4. Discussion

4.1. Depositional History of the Il-Blata Section

Our results show that the depositional environment of the pelagic to hemi-pelagic il-Blata section (Baldassini & Di Stefano, 2015) changed significantly between Depositional Interval 1 and Depositional Interval 2. The lithology shows a change from marine carbonates and episodic phosphorites of Depositional Interval 1, to organic rich calcareous marls (SP IV and VI), fine grained carbonates (SP V) and chert-rich beds (SPVII) of Depositional Interval 2. Another important feature is the extreme change in the sedimentation rate (Figure 5). Depositional Interval 1 contains numerous hiatuses and condensed intervals (Figures 4a–4c and 4e), but an approximate sedimentation rate for the continuous episodes can be estimated from the $^{87}\text{Sr}/^{86}\text{Sr}$ data points at the top and bottom of the uninterrupted deposition for SP II (samples MG 02 and MG 20) and SP III (samples MG 32 and MG 42; Figure 3). These yield low sedimentation rates of $\sim 0.3 \text{ cm kyr}^{-1}$ (SP II) and $\sim 0.1 \text{ cm kyr}^{-1}$ (SP III). The sedimentation rate for Depositional Interval two is 4.7 cm kyr^{-1} and compares well with the published sedimentation rate for the lower part of the MGLm at the St. Thomas outcrop (4.33 cm kyr^{-1}) in the SE of Malta (Figure 2) (Foresi et al., 2014), and is in the same order of magnitude as typical Quaternary pelagic and hemi-pelagic sediments ($1.7\text{--}2.3 \text{ cm kyr}^{-1}$) (Berger et al., 1993). This order of magnitude surge in sedimentation rate indicates a significant change in the depositional environment with a rapid increase in sediment supply and retention. The likely source and paleoenvironmental implications of this enhanced sediment supply are discussed below (Section 4.3).

Depositional Interval one is interpreted to represent deposition in a well-oxygenated and well-mixed water column, subject to significant variations in sea-level and strong episodic upwelling currents. Indications of a periodically well oxygenated water column include the presence of the *Thalassinoides* ichonofacies (Reolid & Betzler, 2019; Savrda & Bottjer, 1989) and the formation of thick phosphatic hardgrounds (Schöllhorn et al., 2019). High amplitude sea-level oscillations are inferred from the general sedimentological pattern of deep water facies capped by erosion surfaces and followed by multiple, cyclic gravity flow deposits (Föllmi et al., 2008) rich in phosphatic material and capped by hardgrounds. The formation of the condensed sections are assumed to be the result of rapid sea-level rises (Baldassini & Di Stefano, 2015). These rapid transgressions are necessary to break pre-existing hardgrounds and carry material by gravity flows down a paleo-slope. These phosphatic hard-grounds are assumed to have been in a paleo-highground in the NW of the present archipelago (Carbone et al., 1987; Pedley & Bennett, 1985). Although we acknowledge the presence of a local tectonic component in the formation of the accommodation space (Dart et al., 1993), this cannot account for the rapid sea-level oscillations. We also note a good match between our Sr/Ca record and the general sedimentological pattern of deep water to shallow water facies with Sr/Ca values decreasing around phosphate-rich intervals and associated hiatuses (Figure 6). In general, Sr/Ca values are relatively low compared with open ocean pelagic carbonates of this age (Billups et al., 2004) which may reflect a more substantial contribution from inorganic calcite. This is consistent with the interpretation of increasing bulk sediment Sr/Ca reflecting increased delivery of aragonite-rich shelf material

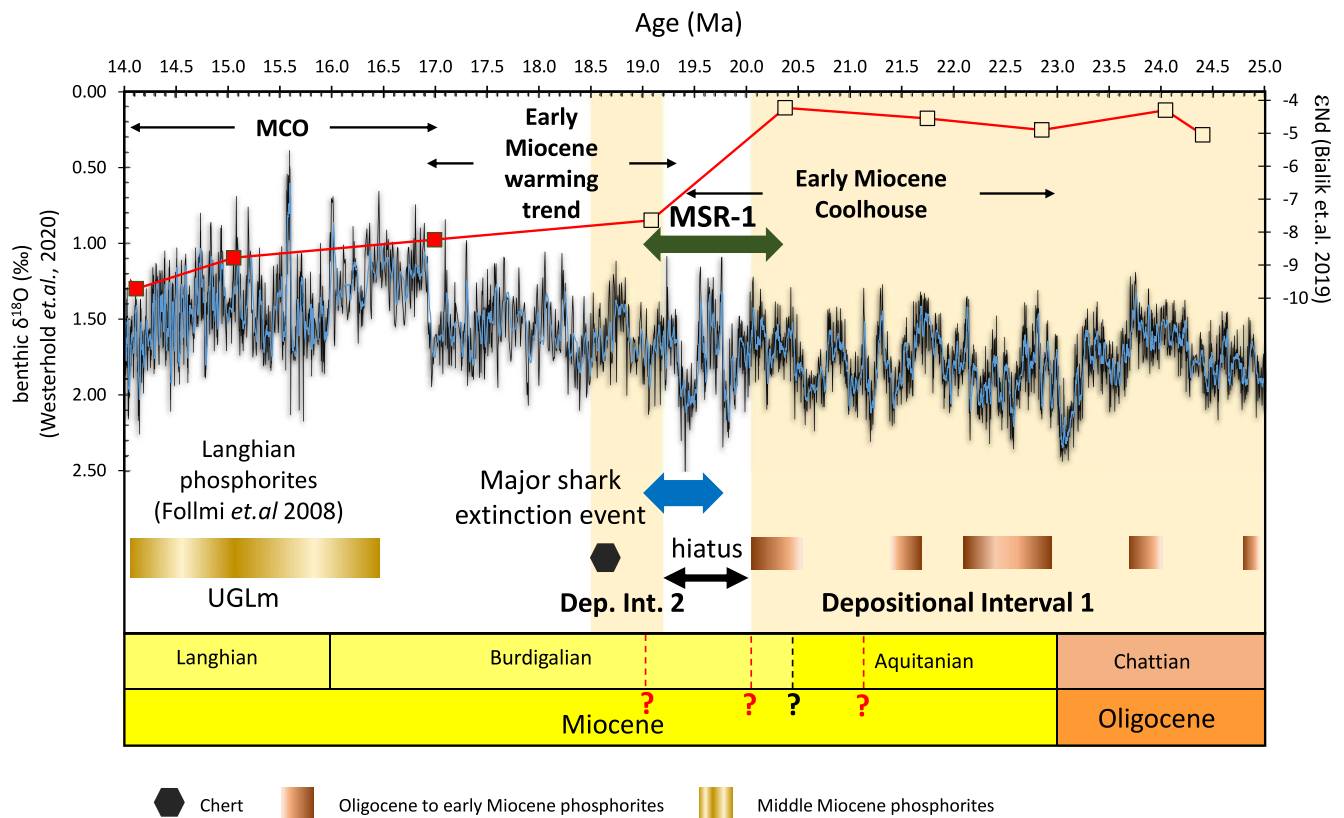


Figure 7. Timing of the Depositional Intervals at il-Blata, Malta compared with sedimentological characteristics, and the timing of the initial restriction of the Mesopotamian Seaway (MSR-1), and a shark extinction event (Sibert & Rubin, 2021). The age of the phosphatic horizons is only a rough approximation owing to the uncertainty in the $^{87}\text{Sr}/^{86}\text{Sr}$ and the non-planar nature of these beds. The age range of the various Langhian phosphorite episodes is from Föllmi et al. (2008). Onset of the chert horizons is marked by black hexagon. Solid symbols in the ϵNd record represent samples collected from other sections in Malta, while open symbols represent samples obtained from the il-Blata section (Bialik et al., 2019) and redated using the age model in this study. The base of the Burdigalian is still a matter of debate (indicated by “?”) with the following four possible values still being considered 21.12, 20.43, 20.04, and 19.03 Ma, with 20.43 being the current stated value (Gradstein et al., 2012; Gradstein et al., 2020).

during sea-level rise and marine transgressions (Bialik et al., 2020; Renard, 1986). The Sr/Ca record for Depositional Interval 2 remains consistently high, reflecting a significant shelf influence, with variations correlatable with the main sedimentary packages (Figure 6). The decrease in % CaCO_3 , the general increase in fine grained sediments (muds and clays) and the surge in sedimentation rate suggests a significantly greater flux of terrigenous material into the area. The fine laminations, absence of bioturbation, dark coloration, scarcity of benthic foraminifera and generally organic-rich lithology within SP IV and VI indicate periods of seafloor suboxia/anoxia.

4.2. Enhanced Siliceous Productivity in a Warming Climate

The depositional system over Malta from the Late Oligocene through the Early Miocene was driven by global glacial-interglacial oscillations. In the earliest Miocene, sedimentation rates and productivity were low, with productivity most likely increasing during phosphorite deposition. The initiation of the phosphatic episodes is associated with eustatic lowstands and the overlying beds are deposited during the subsequent rapid transgression (Baldassini & Di Stefano, 2015). Our Sr/Ca record, age model and lithostratigraphy generally support this idea of a strong association of submarine erosional features, hardgrounds and condensed phosphatic beds with glacial maxima and sea-level lowstand followed by rapid post-glacial transgression (Figures 6 and 7). However, the condensed nature of the phosphatic intervals makes the precise temporal constraint of these episodes difficult and is beyond the scope of this work.

The onset of more humid conditions is associated with increased sedimentation rates, as well as the deposition of more organic- and silica-rich sediments, and follows the MSR—1 step (20.35 to 19.05 Ma) (Figures 5, 7 and 8). The concomitant large increase in Si/Ti indicates that the siliceous/chert interval (SP VII) is dominated

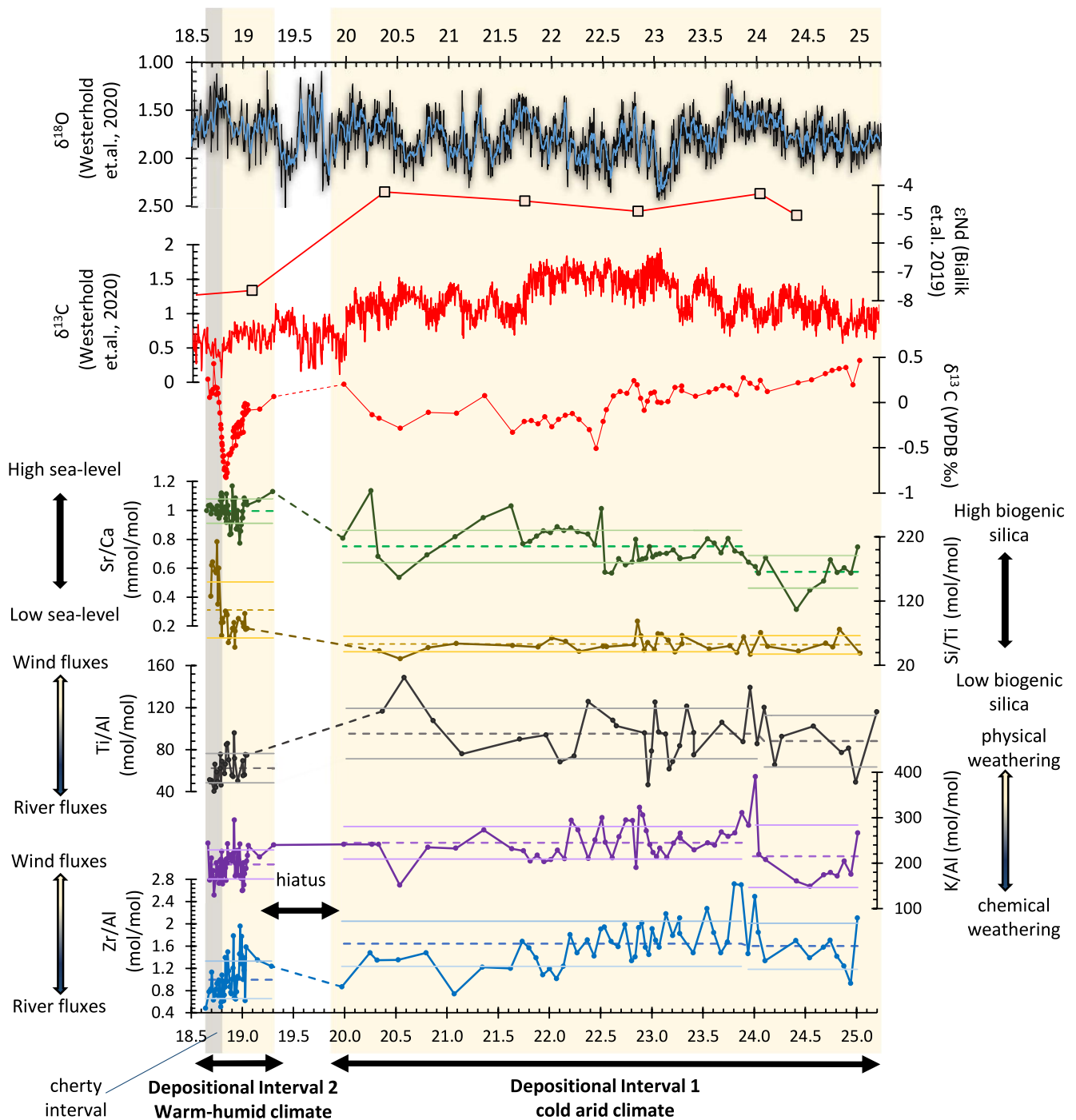


Figure 8. Aluminium normalized proxies Zr/Al, K/Al and Ti/Al used to indicate a decrease in wind-derived sediment fluxes and an increase in chemical weathering following the early Burdigalian hiatus. The surge in Si/Ti indicates an increase in biogenic silica production while the Sr/Ca indicates relative sea-level change at the site of deposition. Dotted line in element ratios indicates mean and coloured lines above and below this indicate 2 s.d. from the mean.

by biogenic production rather than lithogenic input, since an increase in lithogenic silica would most likely also increase the Ti content (Brown et al., 2007) (Figure 8). We interpret this as an increase in biological production in the central Mediterranean during the early Burdigalian. These chert deposits are likely contemporaneous with extensive radiolarian-rich biogenic silica deposits along the Western North African Margin (Ben Yahia et al., 2019; Essid et al., 2019; Riahi et al., 2015) and diatomite-bearing biogenic siliceous beds of Central Italy (Amorosi et al., 1995), although poor age control of these Mediterranean deposits prevent a precise correlation.

The onset of the Miocene Climatic Optimum was marked by a relatively rapid shift to warmer conditions at ~ 17 Ma (Holbourn et al., 2015). However, the benthic oxygen isotope record also indicates an earlier decreasing $\delta^{18}\text{O}$ trend between ~ 19.5 and ~ 17 Ma (Figure 7; De Vleeschouwer et al., 2017; Westerhold et al., 2020) which is correlatable with an Early Miocene warming trend from ~ 20 Ma as indicated by Mg/Ca temperature proxy (Cramer et al., 2011). Widespread decreases in deep ocean CaCO_3 mass accumulation rates have also been used to argue for increasing oceanic dissolved inorganic carbon (DIC) concentrations during this interval, suggesting that the gradual warming was caused by changes in the global carbon cycle (Drury et al., 2021). We note a step increase in chert horizons in the global oceanic records, starting around 19 Ma and terminating around 13 Ma (Muttoni & Kent, 2007). This may suggest that the Early Miocene Mediterranean cherts of Malta, Italy and Tunisia represent a regionally amplified signal of a more global phenomenon during this interval of global warmth. We therefore speculate that this interval of enhanced biogenic silica deposition represents a response to increased delivery of silica and other nutrients to the global oceans. In the Mediterranean region, the chemical weathering of Western North African mountains in a warming climate may have been particularly important (Penman et al., 2019).

4.3. A Hydrologic Shift in the North African Region

The western and central regions of the southern Mediterranean currently receive wind-blown sediment from the Sahara Desert without any significant riverine input from North Africa due to its modern arid climate. During the Holocene, this region was also influenced by riverine fluxes from now extinct fluvial systems that mainly discharged into the Gulf of Sirte (Libya) or the Gulf of Gabez (Tunisia) (Wu et al., 2016, 2017). Sedimentological evidence suggests that Western North African fluvial systems have episodically influenced marine sedimentary environments over Malta as far back as the late Oligocene (Gatt & Gluyas, 2012). In addition, sediments from Mega-Lake Fezzan in western Libya support the existence of an intermittent humid climate by the Early Miocene (23.0 Ma; Hounslow et al., 2017). The influence of fluvial systems in the Mediterranean was thought to have increased around ~ 17 Ma (John et al., 2003), with fully humid conditions in place during the deposition of the Clay Rich Interval (CRI) of the UGLm. However, subsequent age models have suggested that the CRI and hence the establishment of the humid phase occurred later, close to 14.6 Ma (Mourik et al., 2011). Humid conditions further intensified following the MMCT at 13.8 Ma (John et al., 2003). As described above, the change in lithology and sedimentation rate at il-Blata indicates a significantly greater influx of terrigenous material from ~ 19 Ma. The most likely explanation would be a hydrologic shift in the North African region at this time, and we use our multi-proxy records to explore this interpretation below.

4.3.1. An Early Miocene Shift From Aeolian to Fluvial Sediment Fluxes

Aluminium normalized element proxies are here used to support the interpretation of a change in hydrological regime causing the dramatic changes in lithology and sedimentation rate (Figures 5, 6 and 8). The Ti/Al proxy has been successfully applied to represent wind derived sediment fluxes due to dust storms from the Sahara into the Mediterranean during the Pliocene and the Pleistocene (Govin et al., 2012; Lourens et al., 2001). Zr/Al is also indicative of wind-blown Saharan sediment (Martín-Puertas et al., 2010; Martínez-Ruiz et al., 2015). Changes in sea-level would impact the proximity of our study area to the nearest land mass, potentially influencing the accumulation of heavy minerals that contain Ti and Zr. However, the river input for such heavy minerals tends to be very low, and we do not think this is a significant influence on our records (Kumar Warrier & Shankar, 2009). Ti/Al and Zr/Al mainly reflects grain size and hence can differentiate between the intensity of the aeolian/fluvial transport process (Zabel et al., 2001). Potassium is generally associated with the minerals illite and feldspar, both of which are indicative of low rates of chemical weathering and we interpret the K/Al ratio as increasing under arid regimes (high physical weathering) and decreasing under more humid regimes (high chemical weathering) (Govin et al., 2012; Zabel et al., 2001).

There is considerable covariation between the Ti/Al and the Zr/Al records throughout the il-Blata section (Figures 6 and 8) and we interpret the decrease in both these records between Depositional Interval 1 and Depositional Interval 2 as indicating a decrease in wind-blown North African sediment over the central Mediterranean following the early Burdigalian hiatus. The associated increase in sedimentation rate and transition to more clay-rich sediments therefore reflects a shift to a predominantly fluvial sediment supply during the early Burdigalian (after 19.29 Ma), supported by the general decrease in the K/Al record. The shift from a wind dominated to a fluvial dominated sediment supply is consistent with a change from more arid to more humid climate conditions.

4.3.2. Early Miocene Onset of Humid Conditions in North Africa Was Coincident With the Initial Restriction of the Mesopotamian Seaway

A recent study measured bulk sediment ϵNd at il-Blata (using sediments collected by us and published in Bialik et al. (2019)) and other sites, revealing a two-stage restriction of the Mesopotamian Seaway, with the initial restriction occurring in the Early Miocene, and the final restriction associated with the Middle Miocene Climate Transition (Bialik et al., 2019). The scale of change in the ϵNd recorded in Malta cannot be ascribed to a change in weathering regime over North Africa (Bialik et al., 2019). We can therefore confidently correlate MSR-1 with our lithologic and geochemical records, and our improved age model also enables us to better correlate MSR-1 with global records. MSR-1 is marked by a step change in the ϵNd record, reflecting a significantly reduced water flow from the Indian Ocean into the proto-Mediterranean. Our new Sr isotope-based age model suggests that MSR-1 occurred sometime between 20.35 (+0.185, -0.170) Ma and 19.05 (+0.100, -0.100) Ma. It is difficult to refine the chronology further since this interval includes the il-Blata hiatus (19.97 Ma to 19.29 Ma) that separates Depositional Interval 1 and Depositional Interval 2 (Figures 7 and 8). We note that the il-Blata hiatus also coincides with two large positive excursions in the global $\delta^{18}\text{O}$ record with $\delta^{18}\text{O}$ maxima at 19.8 Ma and 19.4 Ma (Figures 7 and 8; Westerhold et al., 2020). These events are assumed to be accompanied by eustatic drops in sea-level, with estimates suggesting sea-level minima of -10 m at 19.8 Ma and -25 m below present day levels at 19.4 Ma (Miller et al., 2020). It is therefore possible that the exact timing of the tectonically induced seaway restriction was also modified by these glacio-eustatic sea level changes. The global planktonic foraminiferal records do not suggest any significant oceanic turnover events at this time (Wade et al., 2011). However, a gap in the Mediterranean planktonic foraminiferal records from 20.66 Ma to 19.74 Ma has been noted, either side of which there appear to be significant changes in abundance of various taxa (Lirer et al., 2019). This could be a sampling gap, but it may also be indicative of a regional hiatus throughout much of the Mediterranean around the Aquitanian/Burdigalian boundary. This interval also coincides with a global mass extinction of pelagic shark populations (>70% of species) between ~20 and ~18 Ma, focused between 19.75 and 19.00 Ma (Sibert & Rubin, 2021). It is therefore striking that the distinct change in depositional regime, representing the onset of more humid conditions in North Africa, is penecontemporaneous with the initial restriction of the Mesopotamian Seaway (Figure 7). We explore the potential mechanisms for this dramatic shift in North African hydrology in Section 4.4.

4.3.3. A Model for the Termination of Late Oligocene to Early Miocene Phosphorite Deposition in the Mediterranean

The initial restriction of the Mesopotamian Seaway was also associated with the termination of the Late Oligocene-Early Miocene phosphorite deposition over Malta and elsewhere. These phosphorite episodes (Schöllhorn et al., 2019) started during the Late Oligocene (28–29 Ma) along the present day United States Pacific coast (Schöllhorn et al., 2019). A belt of phosphorite deposits developed in a west-east trend with major phosphatic episodes occurring during the late Oligocene along the shallow marine coastal areas of California, Mexico (Föllmi et al., 2019; Schöllhorn et al., 2019), Puerto Rico, the Dominican Republic (Ortega-Ariza et al., 2015), and Florida (Schöllhorn et al., 2019). Across the Atlantic, phosphogenesis started later, and by ~25 Ma periodic phosphorite deposits are observed in Malta and Sicily (Carbone et al., 1987; Föllmi et al., 2008; Gruszczynski et al., 2008; Pedley & Bennett, 1985), Central Italy (Auer et al., 2016), and Galicia bank along the Atlantic Spanish/Portuguese submarine coast (González et al., 2016).

These deposits require a combination of global and regional factors to facilitate their formation. From a regional perspective, these include a well-oxygenated water column, strong upwelling systems and low sedimentation rates to allow sufficient time for phosphorite lithification (Schöllhorn et al., 2019). From a global point of view, the rhythmic expansion and contraction of the Antarctic Ice-Sheet and associated glacio-eustatic sea-level oscillations likely facilitated the emplacement of these phosphorite deposits, with the glacial phases forcing wind-driven upwelling systems and the required productivity levels (Schöllhorn et al., 2019). A number of these low latitude phosphogenesis episodes terminate during the Early Miocene (Schöllhorn et al., 2019). The MSR-1-induced changes in Mediterranean circulation would have severely hampered the upwelling systems in the central Mediterranean during glacial maxima (Figure 9; de la Vara and Meijer, 2016). In addition, the more rapid sedimentation on the seafloor would have further inhibited the formation of phosphorites (Föllmi, 1996; Heggie et al., 1990). The global phosphorus cycle is tied to the carbon cycle and can potentially act as a negative or positive feedback on climate change (Föllmi, 1996). However, determining the wider impact of this cessation of regional phosphogenesis requires modeling that is beyond the scope of this paper.

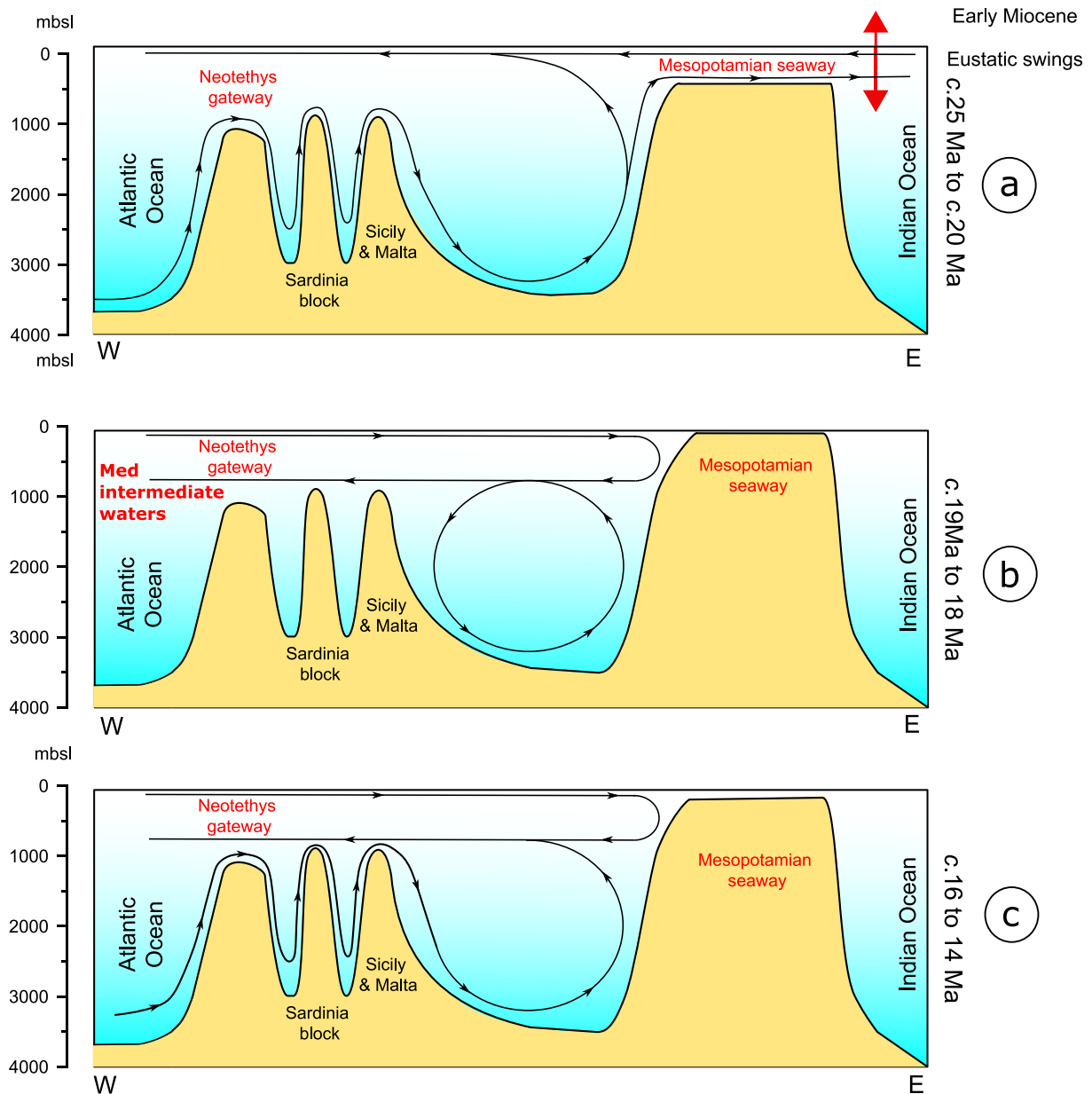


Figure 9. Proposed changes in ocean circulation in the Mediterranean region following the initial restriction of the Mesopotamian Seaway (MSR-1). (a) Between c.25 to 20 Ma, the central Mediterranean would have been subject to episodic upwelling driven by the early Miocene high amplitude glacial-interglacial eustatic sea level changes. During this time interval, episodic allochthonous and autochthonous phosphorites were formed in the central Mediterranean aided by W-E upwelling currents. (b) Following MSR-1, these upwelling systems would have been cut off and warm, saline intermediate waters advected into the Atlantic Ocean. Consequent intensification of the Atlantic thermohaline circulation may have led to an enhanced monsoon system over western North Africa. (c) Possible reconnections may have been re-established during the Miocene Climatic Optimum resulting in re-emergence of phosphatic episodes. Model adapted from (de la Vara and Meijer, 2016).

4.4. A Model for the Onset of a North African Humid Interval in the Early Miocene

The il-Blata hiatus (19.97 to 19.29 Ma) separates a cooler, more arid regional climate regime from subsequent warmer and more humid conditions in the North African region. We consider three possible mechanisms to account for this marked change in North African hydrology: (a) a northward shift in the ITCZ caused by Antarctic cooling, (b) global warmth, and (c) ocean-atmosphere response to water-flow restriction through the Mesopotamian Seaway.

It is thought that the shift of the North African climate from arid to humid during the middle Miocene at 14.6 Ma and subsequent intensification of the hydrological system during the MMCT (13.8 Ma) is likely to have been

due to the northward migration of the ITCZ over Africa as a result of the expansion of the Antarctic Ice-Sheet in a unipolar world (John et al., 2003). We therefore initially consider a similar mechanism for the increased humidity at ~19 Ma. However, the deep sea benthic foraminiferal $\delta^{18}\text{O}$ record suggests reduced global ice volume following 19 Ma (Figure 7; Westerhold et al., 2020), so we discount this possibility as it is difficult to reconcile an increase in global ice volume with a trend toward lower $\delta^{18}\text{O}$ values. The second mechanism therefore is a response to global warmth. The gradual nature of the warming in the benthic foraminiferal $\delta^{18}\text{O}$ record compared with the onset of humid conditions might be used to argue against a global climate driver, although the hydrology of the North African region has been shown to be surprisingly sensitive to regional changes in albedo and vegetation, resulting in tipping point behavior (Demenocal et al., 2000; Hopcroft & Valdes, 2021). Therefore, we consider it is impossible to rule out a global climate driver (e.g., increasing $p\text{CO}_2$) for the increased regional humidity at this time. However, we find it striking that the transition to more humid conditions in North Africa and the termination of phosphorite deposition coincide with the initial restriction of the Mesopotamian Seaway (Figure 7). Prior to the seaway restriction, low-latitude, circum-global circulation had been operating at least since the mid-Cretaceous (~100 Ma; Barron & Peterson, 1989). It is likely that following MSR-1 this low latitude E-W system (Figure 9a) was shut down or severely restricted (Bialik et al., 2019; de la Vara and Meijer, 2016) and that the hot, saline intermediate waters of the proto-Mediterranean started to advect primarily into the Atlantic rather than the Indian Ocean (Figure 9b). This injection of salt may have had a direct effect on Atlantic thermohaline circulation, enhancing the formation of Northern Component Water (NCW; Hamon et al., 2013; Rogerson et al., 2006). We note a shift toward non-radiogenic ϵNd at Ocean Drilling Program (ODP) Site 1090 around this time, possibly reflecting an increasing contribution of Northern Component Water into the Southern Ocean (Scher & Martin, 2008). Enhanced Atlantic thermohaline circulation may in turn have had a significant influence on the strength of the West African monsoon (WAM) by impacting tropical sea surface temperatures and the land-sea gradient (Chang et al., 2008; Latimer & Murray, 2007). Our data demonstrate an increased fluvial sediment supply via North-West African tributaries in the Gulf of Gabes and the Gulf of Sirte, accompanied by surges in sedimentation rate and biogenic silica production in response to a new, distinct climatic regime. We therefore hypothesize that this intensification of the hydrological regime over the region reflects the activation of a weak proto-WAM during the Early Miocene, perhaps favored by the new ocean overturning regime, but we caution that further work is required to investigate these potential couplings.

4.5. Depositional Regimes on Malta Beyond the Il-Blata Section

A lengthy hiatus occurs at il-Blata following the cherty interval SP VII (Baldassini & Di Stefano, 2015, 2017), which may in part be attributed to the complex tectonic history of the Maltese Islands (Dart et al., 1993). Sedimentation continued toward the east of the Maltese Islands with the thick calcareous marls of the Middle Globigerina Limestone member (Foresi et al., 2014), likely indicating that a high productivity regime continued until ~17 Ma and the onset of the MCO. The return of phosphorite deposition in Malta during the interval coinciding with the MCO (Figure 7) (Baldassini & Di Stefano, 2017; Föllmi et al., 2008) indicates that oceanographic conditions favoring phosphorite deposition may have been restored in the central Mediterranean (Figure 9c). One possible mechanism is that the glacio-eustatic sea-level rise associated with the MCO reconnected the Mesopotamian Seaway with the Indian Ocean (Cornacchia et al., 2018), which facilitated periodic upwelling systems within the Mediterranean region (Figure 9c) (de la Vara & Meijer, 2016). These mid-Miocene phosphatic intervals were most likely less active both temporally and spatially than the Late Oligocene to Early Miocene system, as suggested by the absence of hardgrounds and autochthonous phosphorites in Malta and Sicily during this second Miocene phase of phosphogenesis (Föllmi et al., 2008). The onset of the Blue Clay deposition following these phosphorites of the Upper Globigerina Limestone coincides with long term humid conditions over Africa and a permanent global cooling associated with the MMCT (Abels et al., 2005; Hilgen et al., 2009; John et al., 2003).

5. Conclusions

The Early Miocene records from the il-Blata section in the central Mediterranean Island of Malta indicate large regional climatic changes around the base of the Burdigalian (*c.* 19 Ma). A surge in sedimentation rate and aluminium normalized element proxies indicate a marked increase in humidity in the North African region following the Early Miocene restriction of the Mesopotamian Seaway. We suggest that tectonic closure of the Mesopotamian Seaway resulted in the advection of dense, saline waters into the Atlantic, favoring an enhanced

Atlantic thermohaline circulation and altering sea surface temperature patterns. It is possible that consequent changes in ocean-land-atmosphere interactions over the Atlantic activated a humid climatic phase over North Africa, by enhancing the WAM. An alternative mechanism could be a tipping point response to the gradually warming global climate at this time. Regardless of the ultimate cause of the humid climate transition, it seems to have led to significant activation of drainage systems into the central Mediterranean. We suggest that the consequent surge in the delivery flux of terrigenous material, together with the shutting down of W-E upwelling systems, was an important factor in terminating Early Miocene phosphorite depositional systems in this region. Instead, the increased riverine fluxes may have promoted enhanced stratification near the Gulf of Sirte, leading to suboxic/anoxic conditions on the seafloor, and deposition of organic-rich laminated sediments. The high fluxes of terrigenous material in a warmer and wetter climate were likely also associated with increased nutrient supply to the Mediterranean region. This enhanced nutrient supply is seen as the driver for enhanced biological productivity and deposition of silica rich sediments in the central Mediterranean, including the cherty mudstones of the il-Blata section.

The time interval between the first step restriction of the Mesopotamian Seaway (~20 Ma) and the final complete restriction (~14 Ma) was a time of large glacio-eustatic changes and there is a strong possibility of intermittent oceanic reconnection via the Mesopotamian Seaway influencing both the regional Mediterranean climate and the marine depositional environment. Further studies are needed to identify and temporally constrain these reconnection events and link them to changes in the hydrological cycle, and biogeochemical processes in the central Mediterranean. Nevertheless, this work highlights a new potential causal link between the tectonic closure of eastern Tethys and North African hydroclimate, with consequent feedbacks on regional carbon cycle processes.

Data Availability Statement

This research used samples and data generated by the authors. All data presented in this study are given in Tables S1–S6 in Supporting Information S1 and data is archived in PANGAEA—Data Publisher for Earth & Environmental Sciences (Zammit, 2022). Original ϵ Nd Carbonate data is available in the Supplementary Information at Bialik et al. (2019), it is reinterpreted in this study and is available in Table S2 in Supporting Information S1 of the above-mentioned data archived in PANGAEA.

Acknowledgments

This work was funded by the ENDEAVOR Scholarships Scheme (Group B) Malta, Cardiff University, and The Open University Geological Society—Ian Gass bursary (RZ) and NERC grant NE/P019102/1 (CHL). Support is given by Marie Skłodowska Curie Fellowship (101003394-RhodoMalta) (OMB). The Superintendence of Cultural Heritage Malta is thanked for granting permission to collect samples (SCH 213/16). Alexandra Nederbragt, Iain Macdonald and Anthony Oldroyd are thanked for laboratory assistance. John MacArthur is thanked for providing the LOWES-FIT 5 model and useful discussion. This manuscript was improved by the careful comments of two anonymous reviewers and the editor Ursula Röhl.

References

- Abels, H. A., Hilgen, F. J., Krijgsman, W., Kruk, R. W., Raffi, I., Turco, E., & Zachariasse, W. J. (2005). Long-period orbital control on middle Miocene global cooling: Integrated stratigraphy and astronomical tuning of the Blue Clay Formation on Malta. *Paleoceanography*, 20(4). <https://doi.org/10.1029/2004PA001129>
- Abreu, V. S., & Anderson, J. B. (1998). Glacial eustasy during the Cenozoic: Sequence stratigraphic implications. *AAPG Bulletin*, 82(7), 1385–1400. <https://doi.org/10.1306/1D9BCA89-172D-11D7-8645000102C1865D>
- Amorosi, A., Lucchi, F. R., & Tateo, F. (1995). The Lower Miocene siliceous zone: A marker in the palaeogeographic evolution of the northern Apennines. *Palaeogeography, Palaeoclimatology, Palaeoecology*, 118(1–2), 131–149. [https://doi.org/10.1016/0031-0182\(94\)00140-4](https://doi.org/10.1016/0031-0182(94)00140-4)
- Auer, G., Hauzenberger, C. A., Reuter, M., & Piller, W. E. (2016). Orbitally paced phosphogenesis in Mediterranean shallow marine carbonates during the middle Miocene Monterey event. *Geochemistry, Geophysics, Geosystems*, 17(4), 1492–1510. <https://doi.org/10.1002/2016GC006299>
- Badger, M. P. S., Lear, C. H., Pancost, R. D., Foster, G. L., Bailey, T. R., Leng, M. J., & Abels, H. A. (2013). CO₂ drawdown following the middle Miocene expansion of the Antarctic Ice Sheet. *Paleoceanography*, 28(1), 42–53. <https://doi.org/10.1002/palo.20015>
- Baldassini, N., & Di Stefano, A. (2015). New insights on the Oligo-Miocene succession bearing phosphatic layers of the Maltese Archipelago. *Italian Journal of Geoscience*, 134(2), 355–366. <https://doi.org/10.3301/ijg.2014.52>
- Baldassini, N., & Di Stefano, A. (2017). Stratigraphic features of the Maltese Archipelago: A synthesis. *Natural Hazards*, 86, 203–231. <https://doi.org/10.1007/s11069-016-2334-9>
- Barron, E. J., & Peterson, W. H. (1989). Model simulation of the cretaceous ocean circulation. *New Series*, 244(4905), 684–686. <https://doi.org/10.1126/science.244.4905.684>
- Ben Yahia, N., Sebei, A., Harris, C., Boussen, S., & Chaabani, F. (2019). Mineralogical and geochemical criteria to identify the origin and the depositional environment of the upper Numidian babouchite siliceous rocks, northwestern Tunisia. *Journal of African Earth Sciences*, 149, 487–502. <https://doi.org/10.1016/j.jafrearsci.2018.09.010>
- Berger, W. H., Kroenke, L. W., & Mayer, L. A. (1993). 22. Quaternary oxygen isotope record of pelagic foraminifers: Site 806, Ontong Java Plateau 1. *Scientific Results*, 130.
- Bialik, O. M., Frank, M., Betzler, C., Zammit, R., & Waldmann, N. D. (2019). Two-step closure of the Miocene Indian ocean gateway to the Mediterranean. *Scientific Reports*, 9(1), 8842. <https://doi.org/10.1038/s41598-019-45308-7>
- Bialik, O. M., Reolid, J., Betzler, C., Eberli, G. P., & Waldmann, N. D. (2020). Source shifts to periplatform deposits during the early to middle Miocene in response to climatic and oceanographic forcing, Maldives, western Indian Ocean. *Palaeogeography, Palaeoclimatology, Palaeoecology*, 559, 109969. <https://doi.org/10.1016/J.PALAEO.2020.109969>
- Bialik, O. M., Zammit, R., & Micallef, A. (2021). Architecture and sequence stratigraphy of the Upper Coralline Limestone Formation, Malta—Implications for eastern Mediterranean restriction prior to the Messinian salinity crisis. *The Depositional Record*, 7(2), 256–270. <https://doi.org/10.1002/DEP2.138>

- Billups, K., Rickaby, R. E. M., & Schrag, D. P. (2004). Cenozoic pelagic Sr/Ca records: Exploring a link to paleoproductivity. *Paleoceanography*, *19*(3). <https://doi.org/10.1029/2004PA001011>
- Brown, E. T., Johnson, T. C., Scholz, C. A., Cohen, A. S., & King, J. W. (2007). Abrupt change in tropical African climate linked to the bipolar seesaw over the past 55,000 years. *Geophysical Research Letters*, *34*(20), L20702. <https://doi.org/10.1029/2007GL031240>
- Carbone, S., Grasso, M., Lentini, F., & Pedley, H. M. (1987). The distribution and palaeoenvironment of early Miocene phosphorites of southeast Sicily and their relationships with the Maltese phosphorites. *Palaeogeography, Palaeoclimatology, Palaeoecology*, *58*(1–2), 35–53. [https://doi.org/10.1016/0031-0182\(87\)90004-6](https://doi.org/10.1016/0031-0182(87)90004-6)
- Chang, P., Zhang, R., Hazeleger, W., Wen, C., Wan, X., Link, J. I., et al. (2008). Oceanic link between abrupt changes in the North Atlantic Ocean and the African monsoon. <https://doi.org/10.1038/ngeo218>
- Clift, P. D., Wan, S., & Blusztajn, J. (2014). Reconstructing chemical weathering, physical erosion and monsoon intensity since 25Ma in the northern South China Sea: A review of competing proxies. *Earth-Science Reviews*, *130*, 86–102. <https://doi.org/10.1016/j.earscirev.2014.01.002>
- Cornacchia, I., Agostini, S., & Brandano, M. (2018). Miocene oceanographic evolution based on the Sr and Nd isotope record of the central Mediterranean. *Paleoceanography and Paleoclimatology*, *33*(1), 31–47. <https://doi.org/10.1002/2017PA003198>
- Cornacchia, I., Brandano, M., & Agostini, S. (2021). Miocene paleoceanographic evolution of the Mediterranean area and carbonate production changes: A review. *Earth-Science Reviews*, *221*, 103785. <https://doi.org/10.1016/j.earscirev.2021.103785>
- Cramer, B. S., Miller, K. G., Barrett, P. J., & Wright, J. D. (2011). Late Cretaceous–Neogene trends in deep ocean temperature and continental ice volume: Reconciling records of benthic foraminiferal geochemistry ($\delta^{18}\text{O}$ and Mg/Ca) with sea level history. *Journal of Geophysical Research*, *116*(12), C12023. <https://doi.org/10.1029/2011JC007255>
- Cramer, B. S., Toggweiler, J. R., Wright, J. D., Katz, M. E., & Miller, K. G. (2009). Ocean overturning since the Late Cretaceous: Inferences from a new benthic foraminiferal isotope compilation. *Paleoceanography*, *24*(4). <https://doi.org/10.1029/2008PA001683>
- Dart, C. J., Bosence, D. W. J., & McClay, K. R. (1993). Stratigraphy and structure of the Maltese graben system. *Journal of the Geological Society*, *150*(6), 1153–1166. <https://doi.org/10.1144/GSJSIGS.150.6.1153>
- De Vleeschouwer, D., Vahlenkamp, M., Crucifix, M., & Pälike, H. (2017). Alternating Southern and Northern Hemisphere climate response to astronomical forcing during the past 35 m.y. *Geology*, *45*(4), 375–378. <https://doi.org/10.1130/G38663.1>
- de la Vara, A., & Meijer, P. (2016). Response of Mediterranean circulation to Miocene shoaling and closure of the Indian gateway: A model study. *Palaeogeography, Palaeoclimatology, Palaeoecology*, *442*, 96–109. <https://doi.org/10.1016/j.palaeo.2015.11.002>
- Demenocal, P., Ortiz, J., Guilderson, T., Adkins, J., Sarntheim, M., Baker, L., & Yarusinsky, M. (2000). Abrupt onset and termination of the African humid period: Rapid climate responses to gradual insolation forcing. *Quaternary Science Reviews*, *19*(1–5), 347–361. [https://doi.org/10.1016/S0277-3791\(99\)00081-5](https://doi.org/10.1016/S0277-3791(99)00081-5)
- Diester-Haass, L., Billups, K., Gröcke, D. R., François, L., Lefebvre, V., & Emeis, K. C. (2009). Mid-Miocene paleoproductivity in the Atlantic Ocean and implications for the global carbon cycle. *Paleoceanography*, *24*(1). <https://doi.org/10.1029/2008PA001605>
- Diester-Haass, L., Billups, K., Jacquemin, I., Emeis, K. C., Lefebvre, V., & François, L. (2013). Paleoproductivity during the middle Miocene carbon isotope events: A data-model approach. *Paleoceanography*, *28*(2), 334–346. <https://doi.org/10.1002/palo.20033>
- Drury, A. J., Liebrand, D., Westerhold, T., Beddow, H. M., Hodell, D. A., Rohlf, N., et al. (2021). Climate, cryosphere and carbon cycle controls on Southeast Atlantic orbital-scale carbonate deposition since the Oligocene (30–0 Ma). *Climate of the Past*, *17*(5), 2091–2117. <https://doi.org/10.5194/CP-17-2091-2021>
- Essid, J., Saidi, R., Ahmed, A. H., Felhi, M., Fattah, N., & Tlili, A. (2019). Characterization, nomenclature and factors controlling the stability of quartz and opal-CT of Burdigalian and Ypresian siliceous rocks from Tunisia. *Journal of African Earth Sciences*, *155*, 151–160. <https://doi.org/10.1016/j.jafrearsci.2019.04.018>
- Fabbrini, A., Baldassini, N., Caricchi, C., Foresi, L. M., Sagnotti, L., Dinarés-Turell, J., et al. (2019). In search of the Burdigalian GSSP: New evidence from the Contessa Section (Italy). *Italian Journal of Geosciences*, *138*(2), 274–295. <https://doi.org/10.1330/IJG.2019.07>
- Filippidi, A., & De Lange, G. J. (2019). Eastern Mediterranean deep water formation during sapropel S1: A reconstruction using geochemical records along a Bathymetric transect in the Adriatic outflow region. *Paleoceanography and Paleoclimatology*, *34*(3), 409–429. <https://doi.org/10.1029/2018PA003459>
- Flower, B. P., & Kennett, J. P. (1994). The middle Miocene climatic transition: East Antarctic ice sheet development, deep ocean circulation and global carbon cycling. *Palaeogeography, Palaeoclimatology, Palaeoecology*, *108*(3–4), 537–555. [https://doi.org/10.1016/0031-0182\(94\)90251-8](https://doi.org/10.1016/0031-0182(94)90251-8)
- Föllmi, K. B., Gertsch, B., Renevey, J.-P., De Kaenel, E., & Stille, P. (2008). Stratigraphy and sedimentology of phosphate-rich sediments in Malta and south-eastern Sicily (latest Oligocene to early Late Miocene). *Sedimentology*, *55*(4), 1029–1051. <https://doi.org/10.1111/j.1365-3091.2007.00935.x>
- Föllmi, K. B. (1996). The phosphorus cycle, phosphogenesis and marine phosphate-rich deposits. *Earth-Science Reviews*, *40*(1–2), 55–124. [https://doi.org/10.1016/0012-8252\(95\)00049-6](https://doi.org/10.1016/0012-8252(95)00049-6)
- Föllmi, K. B., Gertsch, B., Renevey, J. P., De Kaenel, E., & Stille, P. (2008). Stratigraphy and sedimentology of phosphate-rich sediments in Malta and south-eastern Sicily (latest Oligocene to early Late Miocene). *Sedimentology*, *55*(4), 1029–1051. <https://doi.org/10.1111/j.1365-3091.2007.00935.x>
- Föllmi, K. B., Schöllhorn, I., Ulianov, A., Adatte, T., Spangenberg, J. E., de Kaenel, E., et al. (2019). Phosphogenesis during the Cenozoic transition from greenhouse to icehouse conditions: Upper Oligocene to lower Miocene siliceous, phosphate, and organic-rich sediments near La Purísima, Baja California Sur, Mexico. *The Depositional Record*, *5*(1), 23–52. <https://doi.org/10.1002/dep2.52>
- Foresi, L. M., Baldassini, N., Sagnotti, L., Lirer, F., Di Stefano, A., Caricchi, C., et al. (2014). Integrated stratigraphy of the St. Thomas section (Malta island): A reference section for the lower Burdigalian of the Mediterranean region. *Marine Micropaleontology*, *111*, 66–89. <https://doi.org/10.1016/j.marmicro.2014.06.004>
- Foresi, L. M., Verducci, M., Baldassini, N., Lirer, F., Mazzei, R., Gianfranco, S., et al. (2013). Integrated stratigraphy of St. Peter's pool section (Malta): New age for the upper globigerina limestone member and progress towards the Langhian GSSP.
- Foresi, L. M., Verducci, M., Baldassini, N., Lirer, F., Mazzei, R., Salvatorini, G., et al. (2011). Integrated stratigraphy of St. Peter's Pool section (Malta): New age for the Upper Globigerina Limestone member and progress towards the Langhian GSSP. *Stratigraphy*, *8*(2–3), 125–143.
- Gatt, P. A., & Gluyas, J. G. (2012). Climatic controls on facies in Palaeogene Mediterranean subtropical carbonate platforms. *Petroleum Geoscience*, *18*(3), 355–367. <https://doi.org/10.1144/1354-079311-032>
- González, F. J., Somoza, L., Hein, J. R., Medialdea, T., León, R., Urgorri, V., et al. (2016). Phosphorites, Co-rich Mn nodules, and Fe-Mn crusts from Galicia bank, NE Atlantic: Reflections of Cenozoic tectonics and paleoceanography. *Geochemistry, Geophysics, Geosystems*, *17*(2), 346–374. <https://doi.org/10.1002/2015GC005861>
- Govin, A., Holzwarth, U., Heslop, D., Keeling, L. F., Zabel, M., Mulitza, S., et al. (2012). Distribution of major elements in Atlantic surface sediments (36°N–49°S): Imprint of terrigenous input and continental weathering. *Geochemistry, Geophysics, Geosystems*, *13*(1). <https://doi.org/10.1029/2011GC003785>

- Gradstein, F. M., Ogg, J. G., & Hilgen, F. J. (2012). On the geologic time scale. *Newsletters on Stratigraphy*, 45(2), 171–188. <https://doi.org/10.1127/0078-0421/2012/0020>
- Gradstein, F. M., Ogg, J. G., Schmitz, M., & Ogg, G. (2020). *Geologic time scale 2020*, Elsevier. <https://doi.org/10.1016/C2020-1-02369-3>
- Gruszczynski, M., Marshall, J. D., Goldring, R., Coleman, M. L., Malkowski, K., Gazdzicka, E., et al. (2008). Hiatal surfaces from the Miocene Globigerina Limestone Formation of Malta: Biostratigraphy, sedimentology, trace fossils and early diagenesis. *Palaeoecology, Palaeoclimatology, Palaeoecology*, 270(3–4), 239–251. <https://doi.org/10.1016/j.palaeo.2008.01.035>
- Hamon, N., Sepulchre, P., Lefebvre, V., & Ramstein, G. (2013). Climate of the past the role of eastern Tethys seaway closure in the middle Miocene climatic transition (ca. 14 Ma). *Climate of the Past*, 9(6), 2687–2702. <https://doi.org/10.5194/cp-9-2687-2013>
- Heggie, D. T., Skyring, G. W., O'Brien, G. W., Reimers, C., Herczeg, A., Moriarty, D. J. W., et al. (1990). Organic carbon cycling and modern phosphorite formation on the East Australian continental margin: An overview. *Geological Society, London, Special Publications*, 52(1), 87–117. <https://doi.org/10.1144/GSL.SP.1990.052.01.07>
- Hennekam, R., Donders, T. H., Zwiep, K., & de Lange, G. J. (2015). Integral view of Holocene precipitation and vegetation changes in the Nile catchment area as inferred from its delta sediments. *Quaternary Science Reviews*, 130, 189–199. <https://doi.org/10.1016/j.quascirev.2015.05.031>
- Hilgen, F. J., Abels, H. A., Iaccarino, S., Krijgsman, W., Raffi, I., Sprovieri, R., et al. (2009). The global stratotype section and point (GSSP) of the serravallian stage (middle Miocene). *Episodes*, 32(3), 152–166. Retrieved from http://apps.webofknowledge.com.abc.cardiff.ac.uk/full_record.do?product=WOS%26search_mode=GeneralSearch%26qid=1%26SID=W2cpShHo7sIw7FxDalX%26page=1%26doc=1
- Holbourn, A., Kuhnt, W., Kochhann, K. G. D., Andersen, N., & Sebastian Meier, K. J. (2015). Global perturbation of the carbon cycle at the onset of the Miocene Climatic Optimum. *Geology*, 43(2), 123–126. <https://doi.org/10.1130/G36317.1>
- Holbourn, A., Kuhnt, W., Lyle, M., Schneider, L., Romero, O., & Andersen, N. (2014). Middle Miocene climate cooling linked to intensification of eastern equatorial Pacific upwelling. *Geology*, 42(1), 19–22. <https://doi.org/10.1130/G34890.1>
- Holbourn, A., Kuhnt, W., Schulz, M., Flores, J.-A., & Andersen, N. (2007). Orbitally-paced climate evolution during the middle Miocene “Monterey” carbon-isotope excursion. <https://doi.org/10.1016/j.epsl.2007.07.026>
- Hopcroft, P. O., & Valdes, P. J. (2021). Paleoclimate-conditioning reveals a North Africa land-atmosphere tipping point. *Proceedings of the National Academy of Sciences of United States of America*, 118(45), e2108783118. <https://doi.org/10.1073/PNAS.2108783118>
- Hounslow, M. W., White, H. E., Drake, N. A., Salem, M. J., El-Hawat, A., McLaren, S. J., et al. (2017). Miocene humid intervals and establishment of drainage networks by 23 Ma in the central Sahara, southern Libya. *Gondwana Research*, 45, 118–137. <https://doi.org/10.1016/J.GR.2016.11.008>
- Iaccarino, S. M., Di Stefano, A., Foresi, L. M., Turco, E., Baldassini, N., Cascella, A., et al. (2011). High-resolution integrated stratigraphy of the upper Burdigalian-lower Langhian in the Mediterranean: The Langhian historical stratotype and new candidate sections for defining its GSSP. *Stratigraphy*, 8(2–3), 199–215.
- Jacobs, E., Weissert, H., Shields, G., & Stille, P. (1996). The Monterey event in the Mediterranean: A record from shelf sediments of Malta. *Paleoceanography*, 11(6), 717–728. <https://doi.org/10.1029/96PA02230>
- John, C. M., Mutti, M., & Adatte, T. (2003). Mixed carbonate-siliciclastic record on the North African margin (Malta)—Coupling of weathering processes and mid Miocene climate. *The Geological Society of America Bulletin*, 115(2), 217–229. [https://doi.org/10.1130/0016-7606\(2003\)115<0217:MCSROT>2.0.CO;2](https://doi.org/10.1130/0016-7606(2003)115<0217:MCSROT>2.0.CO;2)
- Kocsis, L., Vennemann, D., Fontignie, D., Baumgartner, C., Montanari, A., & Jelen, B. (2008). Oceanographic and climatic evolution of the Miocene Mediterranean deduced from Nd, Sr, C, and O isotope compositions of marine fossils and sediment. *Paleoceanography*, 23(4), 4211. <https://doi.org/10.1029/2007PA001540>
- Krom, M. D., Michard, A., Cliff, R. A., & Strohle, K. (1999). Sources of sediment to the Ionian sea and Western Levantine basin of the eastern Mediterranean during S-1 sapropel times. *Marine Geology*, 160(1–2), 45–61. [https://doi.org/10.1016/S0025-3227\(99\)00015-8](https://doi.org/10.1016/S0025-3227(99)00015-8)
- Kumar Warrior, A., & Shankar, R. (2009). Geochemical evidence for the use of magnetic susceptibility as a paleorainfall proxy in the tropics. <https://doi.org/10.1016/j.chemgeo.2009.05.023>
- Kylander, M. E., Ampel, L., Wohlfarth, B., & Veres, D. (2011). High-resolution X-ray fluorescence core scanning analysis of Les Echets (France) sedimentary sequence: New insights from chemical proxies. *Journal of Quaternary Science*, 26(1), 109–117. <https://doi.org/10.1002/JQS.1438>
- Latimer, J. C., Murray, R. W., & Flores, J. A. (2007). Productivity records from the southern Ocean and the equatorial Pacific ocean: Testing the glacial shelf-nutrient hypothesis. *Deep Sea Research Part II: Topical Studies in Oceanography*, 54(21–22), 2443–2452. <https://doi.org/10.1016/J.DSR2.2007.07.021>
- Lear, C. H., Coxall, H. K., Foster, G. L., Lunt, D. J., Mawbey, E. M., Rosenthal, Y., et al. (2015). Neogene ice volume and ocean temperatures: Insights from infaunal foraminiferal Mg/Ca paleothermometry. *Paleoceanography*, 30(11), 1437–1454. <https://doi.org/10.1002/2015PA002833>
- Lewis, L., & Christensen, A. M. (2016). Effects of aluminium foil packaging on elemental analysis of Bone. *Journal of Forensic Sciences*, 61(2), 439–441. <https://doi.org/10.1111/1556-4029.12994>
- Liebrand, D., Lourens, L. J., Hodell, D. A., de Boer, B., van de Wal, R. S. W., & Paellike, H. (2011). Antarctic ice sheet and oceanographic response to eccentricity forcing during the early Miocene. *Climate of the Past*, 7(3), 869–880. <https://doi.org/10.5194/cp-7-869-2011>
- Lirer, F., Foresi, L. M., Iaccarino, S. M., Salvatorini, G., Turco, E., Cosentino, C., et al. (2019). Mediterranean Neogene planktonic foraminifer biozonation and biochronology. *Earth-Science Reviews*, 196, 102869. <https://doi.org/10.1016/J.EARSCIREV.2019.05.013>
- Lourens, L. J., Wehausen, R., & Brumsack, H. J. (2001). Geological constraints on tidal dissipation and dynamical ellipticity of the Earth over the past three million years. *Nature*, 409, 6823–1033. <https://doi.org/10.1038/35059062>
- Martínez-Ruiz, F., Kastner, M., Gallego-Torres, D., Rodrigo-Gámiz, M., Nieto-Moreno, V., & Ortega-Huertas, M. (2015). Paleoclimate and paleoceanography over the past 20,000yr in the Mediterranean Sea Basins as indicated by sediment elemental proxies. *Quaternary Science Reviews*, 107, 25–46. <https://doi.org/10.1016/j.quascirev.2014.09.018>
- Martín-Puertas, C., Jiménez-Espejo, F., Martínez-Ruiz, F., Nieto-Moreno, V., Rodrigo, M., Mata, M. P., & Valero-Garcés, B. L. (2010). Late Holocene climate variability in the southwestern Mediterranean region: An integrated marine and terrestrial geochemical approach. *Climate of the Past*, 6(6), 807–816. <https://doi.org/10.5194/CP-6-807-2010>
- Masson-Delmotte, V., Zhai, P., Pirani, S. L., Connors, C., Péan, C., & Berger, S., (2021). *IPCC 2021: Climate Change 2021: The Physical Science Basis. Contribution of Working Group I to the Sixth Assessment Report of the Intergovernmental Panel on Climate Change*. Cambridge University Press.
- Mawbey, E. M., & Lear, C. H. (2013). Carbon cycle feedbacks during the Oligocene-Miocene transient glaciation. *Geology*, 41(9), 963–966. <https://doi.org/10.1130/G34422.1>
- McArthur, J. M., Howarth, R. J., & Bailey, T. R. (2001). Strontium isotope stratigraphy: LOWESS version 3: Best fit to the marine Sr-isotope curve for 0–509 Ma and accompanying Look-up table for deriving numerical age. *The Journal of Geology*, 109(2), 155–170. <https://doi.org/10.1086/319243>

- McArthur, J. M., Howarth, R. J., & Shields, G. A. (2012). Strontium isotope stratigraphy. *The Geologic Time Scale*, 127–144. <https://doi.org/10.1016/B978-0-444-59425-9.00007-X>
- Miller, K. G., Browning, J. V., Schmelz, W. J., Kopp, R. E., Mountain, G. S., & Wright, J. D. (2020). Cenozoic sea-level and cryospheric evolution from deep-sea geochemical and continental margin records. *Science Advances*, 6(20), eaaz1346. <https://doi.org/10.1126/sciadv.aaz1346>
- Miller, K. G., Wright, J. D., & Fairbanks, R. G. (1991). Unlocking the ice house—Oligocene-Miocene oxygen isotopes, eustasy, and margin erosion. *Journal of Geophysical Research: Solid Earth and Planets*, 96(B4), 6829–6848. <https://doi.org/10.1029/90JB02015>
- Mourik, A. A., Abels, H. A., Hilgen, F. J., Di Stefano, A., & Zachariasse, W. J. (2011). Improved astronomical age constraints for the middle Miocene climate transition based on high-resolution stable isotope records from the central Mediterranean Maltese Islands. *Paleoceanography*, 26(1), PA1210. <https://doi.org/10.1029/2010PA001981>
- Mudelsee, M., Bickert, T., Lear, C. H., & Lohmann, G. (2014). Cenozoic climate changes: A review based on time series analysis of marine benthic $\delta^{18}O$ records. *Reviews of Geophysics*, 52(3), 333–374. <https://doi.org/10.1002/2013RG000440>
- Mutti, M., John, C. M., & Knoerich, A. C. (2006). Chemostratigraphy in Miocene heterozoan carbonate settings: Applications, limitations and perspectives. *Geological Society, London, Special Publications*, 255(1), 307–322. <https://doi.org/10.1144/GSL.SP.2006.255.01.18>
- Muttoni, G., & Kent, D. V. (2007). Widespread formation of cherts during the early Eocene climate optimum. *Palaeogeography, Palaeoclimatology, Palaeoecology*, 253(3–4), 348–362. <https://doi.org/10.7916/D8S75RVS>
- Naish, T. R., Woolfe, K. J., Barrett, P. J., Wilson, G. S., Atkins, C., Bohaty, S. M., et al. (2001). Orbitally induced oscillations in the East Antarctic ice sheet at the Oligocene/Miocene boundary. *Nature*, 413(6857), 719–723. <https://doi.org/10.1038/35099534>
- Oehlert, A. M., & Swart, P. K. (2014). Article Interpreting carbonate and organic carbon isotope covariance in the sedimentary record. *Nature Communications*, 5(1), 4672. <https://doi.org/10.1038/ncomms5672>
- Ortega-Ariza, D., Franseen, E. K., Santos-Mercado, H., Ramírez-Martínez, W. R., & Core-Suárez, E. E. (2015). Strontium isotope stratigraphy for Oligocene-Miocene carbonate systems in Puerto Rico and the Dominican republic: Implications for Caribbean processes affecting depositional history. *The Journal of Geology*, 123(6), 539–560. <https://doi.org/10.1086/683335>
- Passier, H. F., & de Lange, G. J. (1998). 20. *Sedimentary sulfur and iron chemistry in relation to the formation of eastern Mediterranean sapropels 1*. Scientific Results.160
- Pedley, H. M., & Bennett, S. M. (1985). Phosphorites, hardgrounds and syndepositional solution subsidence: A palaeoenvironmental model from the Miocene of the Maltese islands. In *Sedimentary geology*. [https://doi.org/10.1016/0037-0738\(85\)90022-3](https://doi.org/10.1016/0037-0738(85)90022-3)
- Penman, D. E., Keller, A., D'haenens, S., Turner, S. K., & Hull, P. M. (2019). Atlantic deep-sea cherts associated with Eocene hyperthermal events. *Paleoceanography and Paleoclimatology*, 34(2), 287–299. <https://doi.org/10.1029/2018PA003503>
- Potter, P. E., & Szatmari, P. (2009). Global Miocene tectonics and the modern world. *Earth-Science Reviews*, 96(4), 279–295. <https://doi.org/10.1016/j.earscirev.2009.07.003>
- Renard, M. (1986). Pelagic carbonate chemostratigraphy (Sr, Mg, ^{18}O , ^{13}C). *Marine Micropaleontology*, 10(1–3), 117–164. [https://doi.org/10.1016/0377-8398\(86\)90027-7](https://doi.org/10.1016/0377-8398(86)90027-7)
- Reolid, J., & Betzler, C. (2019). The ichnology of carbonate drifts. *Sedimentology*, 66(4), 1427–1448. <https://doi.org/10.1111/SED.12563>
- Riahi, S., Soussi, M., & Ben Ismail Latrache, K. (2015). Age, internal stratigraphic architecture and structural style of the Oligocene-Miocene Numidian formation of northern Tunisia. *Annales Societatis Geologorum Poloniae*, 85(2), 345–370. <https://doi.org/10.14241/ASGP.2015.009>
- Rogerson, M., Rohling, E. J., & Weaver, P. P. E. (2006). Promotion of meridional overturning by Mediterranean-derived salt during the last deglaciation. *Paleoceanography*, 21(4). <https://doi.org/10.1029/2006PA001306>
- Rögl, F. (1999). Mediterranean and paratethys. Facts and hypotheses of an Oligocene to Miocene paleogeography (Short overview). *Geologica Carpathica*, 50, 339–349.
- Savrdra, C. E., & Bottjer, D. J. (1989). Trace-fossil model for reconstructing oxygenation histories of ancient marine bottom waters: Application to Upper Cretaceous Niobrara Formation, Colorado. *Palaeogeography, Palaeoclimatology, Palaeoecology*, 74(1–2), 49–74. [https://doi.org/10.1016/0031-0182\(89\)90019-9](https://doi.org/10.1016/0031-0182(89)90019-9)
- Scher, H. D., & Martin, E. E. (2008). Oligocene deep water export from the North Atlantic and the development of the Antarctic Circumpolar Current examined with neodymium isotopes. *Paleoceanography*, 23(1). <https://doi.org/10.1029/2006PA001400>
- Schöllhorn, I., Houben, A., Gertsch, B., Adatte, T., Alexey, U., de Kaenel, E., et al. (2019). Enhanced upwelling and phosphorite formation in the northeastern Pacific during the late Oligocene: Depositional mechanisms, environmental conditions, and the impact of glacio-eustasy. *GSA Bulletin*, 132(3–4), 687–709. <https://doi.org/10.1130/B32061.1>
- Sibert, E. C., & Rubin, L. D. (2021). An early Miocene extinction in pelagic sharks. *Science*, 372(6546), 1105–1107. <https://doi.org/10.5061/dryad>
- Sosdian, S. M., Babila, T. L., Greenop, R., Foster, G. L., & Lear, C. H. (2020). Ocean carbon storage across the middle Miocene: A new interpretation for the monterey event. *Nature Communications*, 11(1), 134. <https://doi.org/10.1038/s41467-019-13792-0>
- Steinthorsdóttir, M., Coxall, H. K., De Boer, A. M., Huber, M., Barbolini, N., Bradshaw, C. D., et al. (2020). The Miocene: The future of the past citation: Special section: The Miocene: The future of the past paleoceanography and paleoclimatology. <https://doi.org/10.1029/2020PA004037>
- Sun, J., Sheykh, M., Ahmadi, N., Cao, M., Zhang, Z., Tian, S., et al. (2021). Permanent closure of the Tethyan Seaway in the northwestern Iranian Plateau driven by cyclic sea-level fluctuations in the late Middle Miocene. *Palaeogeography, Palaeoclimatology, Palaeoecology*, 564, 110172. <https://doi.org/10.1016/j.palaeo.2020.110172>
- Vincent, E., & Berger, W. H. (1985). *Carbon dioxide and polar cooling in the Miocene: The monterey hypothesis* (pp. 455–468). The Carbon Cycle and Atmospheric CO. <https://doi.org/10.1029/GM032P0455>
- Wade, B. S., Pearson, P. N., Berggren, W. A., & Pälike, H. (2011). Earth-Science Reviews Review and revision of Cenozoic tropical planktonic foraminiferal biostratigraphy and calibration to the geomagnetic polarity and astronomical time scale. *Earth-Science Reviews*, 104(1–3), 111–142. <https://doi.org/10.1016/j.earscirev.2010.09.003>
- Wei, G.-J., Zou, L., Deng, W.-F., Li, X.-H., Liu, Y., & Chen, J.-F. (2009). Mn/Ca ratio in planktonic foraminifer from ODP site 1144, the northern south China sea: A possible paleoclimate indicator. *Geochemical Journal*, 43(4), 235–246. <https://doi.org/10.2343/geochemj.1.0031>
- Westerhold, T., Marwan, N., Drury, A. J., Liebrand, D., Agnini, C., Anagnostou, E., et al. (2020). An astronomically dated record of Earth's climate and its predictability over the last 66 million years. *American Association for the Advancement of Science*, 369(6509), 1383–1388. <https://doi.org/10.1126/SCIENCE.ABA6853>
- Wu, J., Böning, P., Pahnke, K., Tachikawa, K., & de Lange, G. J. (2016). Unraveling North-African riverine and eolian contributions to central Mediterranean sediments during Holocene sapropel S1 formation. *Quaternary Science Reviews*, 152, 31–48. <https://doi.org/10.1016/j.quascirev.2016.09.029>
- Wu, J., Liu, Z., Stuu, J. B. W., Zhao, Y., Schirone, A., & de Lange, G. J. (2017). North-African paleodrainage discharges to the central Mediterranean during the last 18,000 years: A multiproxy characterization. *Quaternary Science Reviews*, 163, 95–113. <https://doi.org/10.1016/j.quascirev.2017.03.015>

- Zabel, M., Schneider, R. R., Wagner, T., Adegbe, A. T., De Vries, U., & Kolonic, S. (2001). Late quaternary climate changes in central Africa as inferred from terrigenous input to the Niger fan. *Quaternary Research*, *56*(2), 207–217. <https://doi.org/10.1006/QRES.2001.2261>
- Zachos, J., Pagani, M., Sloan, L., Thomas, E., & Billups, K. (2001). Trends, rhythms, and aberrations in global climate 65 Ma to present. *Science*, *292*(5517), 686–693. <https://doi.org/10.1126/science.1059412>
- Zammit, R. (2022). Early miocene intensification of the North African hydrological cycle: Multi-proxy evidence from the shelf carbonates of Malta - geochemical data. Pangaea, [Dataset]. oi: <https://doi.org/10.1594/PANGAEA.947547>